ADVANCING EARTH AND SPACE SCIENCES

JAMES | Journal of Advances in Modeling Earth Systems®

RESEARCH ARTICLE
10.1029/2022MS003505

A Method for Estimating Global Subgrid-Scale Orographic Gravity-Wave Temperature Perturbations in Chemistry-Climate Models

M. Weimer[1,2], C. Wilka[1,3], D. E. Kinnison[4], R. R. Garcia[4], J. T. Bacmeister[5], M. J. Alexander[6], A. Dörnbrack[7], and S. Solomon[1]

[1]Department of Earth, Atmospheric and Planetary Sciences, Massachusetts Institute of Technology, Cambridge, MA, USA, [2]Now at Institute of Environmental Physics, University of Bremen, Bremen, Germany, [3]Department of Earth System Science, Stanford University, Stanford, CA, USA, [4]Atmospheric Chemistry Observations & Modeling Laboratory, National Center for Atmospheric Research, Boulder, CO, USA, [5]Climate and Global Dynamics Laboratory, National Center for Atmospheric Research, Boulder, CO, USA, [6]NorthWest Research Associates/Colorado Research Associates, Boulder, CO, USA, [7]Institut für Physik der Atmosphäre, Deutsches Zentrum für Luft und Raumfahrt, Oberpfaffenhofen, Germany

Key Points:

- We present a method for estimating subgrid-scale orographic gravity wave temperature perturbations on a global scale
- The distributions of these perturbations are compared with Constellation Observing System for Meteorology Ionosphere and Climate/Formosa Satellite 3 and ECMWF Reanalysis version 5 to estimate scaling factors
- These temperature perturbations impact stratospheric aerosols and chemistry particularly near the tropical tropopause and polar regions

Supporting Information:

Supporting Information may be found in the online version of this article.

Correspondence to:

M. Weimer,
mweimer@mit.edu

Citation:

Weimer, M., Wilka, C., Kinnison, D. E., Garcia, R. R., Bacmeister, J. T., Alexander, M. J., et al. (2023). A method for estimating global subgrid-scale orographic gravity-wave temperature perturbations in chemistry-climate models. *Journal of Advances in Modeling Earth Systems*, *15*, e2022MS003505. https://doi.org/10.1029/2022MS003505

Received 4 NOV 2022
Accepted 13 AUG 2023

Author Contributions:

Conceptualization: M. Weimer, S. Solomon
Data curation: D. E. Kinnison
Formal analysis: R. R. Garcia, J. T. Bacmeister, M. J. Alexander, S. Solomon

Abstract Many chemical processes depend non-linearly on temperature. Gravity-wave-induced temperature perturbations have been shown to affect atmospheric chemistry, but accounting for this process in chemistry-climate models has been a challenge because many gravity waves have scales smaller than the typical model resolution. Here, we present a method to account for subgrid-scale orographic gravity-wave-induced temperature perturbations on the global scale for the Whole Atmosphere Community Climate Model. Temperature perturbation amplitudes $\hat{T}$ consistent with the model's subgrid-scale gravity wave parameterization are derived and then used as a sinusoidal temperature perturbation in the model's chemistry solver. Because of limitations in the parameterization, we explore scaling of $\hat{T}$ between 0.6 and 1 based on comparisons to altitude-dependent $\hat{T}$ distributions of satellite and reanalysis data, where we discuss uncertainties. We probe the impact on the chemistry from the grid-point to global scales, and show that the parameterization is able to represent mountain wave events as reported by previous literature. The gravity waves for example, lead to increased surface area densities of stratospheric aerosols. This increases chlorine activation, with impacts on the associated chemical composition. We obtain large local changes in some chemical species (e.g., active chlorine, NO_x, N_2O_5) which are likely to be important for comparisons to airborne or satellite observations, but the changes to ozone loss are more modest. This approach enables the chemistry-climate modeling community to account for subgrid-scale gravity wave temperature perturbations interactively, consistent with the internal parameterizations and are expected to yield more realistic interactions and better representation of the chemistry.

Plain Language Summary Sub-grid scale gravity waves have long been incorporated in the momentum budgets of global chemistry-climate models using parameterizations, but their associated impacts on temperature dependent chemistry within the models have not been included in a self-consistent way. Here we present an approach to modeling these chemical impacts in the Whole Atmosphere Community Climate Model. We obtain large local changes in some chemical species (e.g., active chlorine, NO_x, N_2O_5) but smaller impacts on ozone. The approach can be expected to advance the ability of the chemistry-climate modeling community to examine gravity wave effects on a wide range of chemical problems.

1. Introduction

A number of chemical processes in the atmosphere are non-linearly dependent on the temperature. For instance, chemical reactions often depend exponentially on the temperature (Burkholder et al., 2015), and the formation of stratospheric aerosols is linked to temperature thresholds (Carslaw et al., 1994; Eckermann et al., 2006; Hanson & Mauersberger, 1988; Marti & Mauersberger, 1993; Solomon et al., 2015). As a consequence, small-scale variations of the temperature, that arise for example, from wave-like perturbations, can change the concentrations of atmospheric trace gases despite an unchanged averaged temperature across the wave motion since

$$k\left(\overline{T}\right) \neq \overline{k(T)} \tag{1}$$

Funding acquisition: S. Solomon
Investigation: M. Weimer, R. R. Garcia, S. Solomon
Methodology: M. Weimer, C. Wilka, R. R. Garcia, J. T. Bacmeister, M. J. Alexander, A. Dörnbrack, S. Solomon
Project Administration: S. Solomon
Resources: M. Weimer, D. E. Kinnison, R. R. Garcia, S. Solomon
Software: M. Weimer, C. Wilka, D. E. Kinnison, J. T. Bacmeister, A. Dörnbrack
Supervision: S. Solomon
Validation: M. Weimer, M. J. Alexander
Visualization: M. Weimer, C. Wilka, J. T. Bacmeister
Writing – original draft: M. Weimer, S. Solomon
Writing – review & editing: C. Wilka, D. E. Kinnison, R. R. Garcia, J. T. Bacmeister, M. J. Alexander, A. Dörnbrack, S. Solomon

where k is a heterogeneous or gas-phase reaction rate constant and T is temperature (e.g., Murphy & Ravishankara, 1994). Even small-scale temperature perturbations can lead to large (at least local) differences in the chemistry due to the mentioned non-linearities and should in principle be accounted for in chemistry-climate models. Examples of waves leading to such temperature perturbations include Kelvin, Rossby and gravity waves (Das & Pan, 2013; Fritts & Alexander, 2003; Madden, 1979). While the planetary scale Kelvin and Rossby waves can be resolved by current chemistry-climate models (Eyring et al., 2016; Knippertz et al., 2022), a significant fraction of the gravity wave spectrum occurs on the subgrid scales of current models (e.g., Fritts & Alexander, 2003; Garcia et al., 2017; Giorgetta et al., 2018).

Gravity waves are generated by various sources including orography and convection, and can propagate horizontally and vertically in a stably stratified atmosphere. These waves have been shown to affect the atmosphere's dynamical structure, especially the stratosphere and mesosphere (see Fritts & Alexander, 2003, for an overview). Here, we focus on orographic gravity waves (OGWs). Many regions of enhanced OGW amplitudes (a.k.a. "hot spots") have been identified at high latitudes via various measurement techniques: the Scandinavian Mountains, Iceland, Svalbard, Greenland, Ural Mountains, Rocky Mountains and the Himalayas in the Northern Hemisphere and the Andes, the Antarctic Peninsula, the Transantarctic Mountains, New Zealand and various small islands in the Southern Hemisphere (S. P. Alexander et al., 2009; Dörnbrack et al., 2017; Hoffmann et al., 2013; Jackson et al., 2018; Kaifler et al., 2020; Krisch et al., 2017; Lilly et al., 1982; Rapp et al., 2021; Taylor et al., 2019; Vosper et al., 2020).

Properties of gravity waves can be measured by satellite instruments on a global scale (Anthes et al., 2008; Hoffmann & Alexander, 2009) and locally by radiosondes, instrumented aircrafts, or lidar instruments (e.g., Kaifler et al., 2020; Leena et al., 2012; Rapp et al., 2021). Radio occultation satellite measurements, such as those by the Constellation Observing System for Meteorology Ionosphere and Climate/Formosa Satellite 3 (COSMIC) mission (Anthes et al., 2008), have been shown to provide high-precision measurements of gravity wave temperature perturbations with daily global coverage (e.g., L. Wang & Alexander, 2010). In addition, recent reanalysis products like the ECMWF Reanalysis version 5 (ERA5) have been shown to resolve parts of the gravity wave spectrum (Dörnbrack, 2021; Dörnbrack et al., 2020, 2022; Gupta et al., 2021; Hoffmann et al., 2019; Rapp et al., 2021). Stratospheric gravity wave-driven temperature perturbations as large as 45 K have been measured (Hindley et al., 2021). The subgrid-scale effects of such waves on the momentum budget are a necessary component of global climate models (e.g., Bacmeister et al., 1994; Fritts & Alexander, 2003; Garcia et al., 2017; Giorgetta et al., 2018; Kruse et al., 2022), providing the framework needed to examine their associated impacts on the global chemistry.

Accounting for the impact of gravity-wave-induced temperature perturbations on polar stratospheric clouds (PSCs) and the chemistry in atmospheric models has been a subject of scientific focus for several decades. Lagrangian models have been used to successfully simulate the formation of PSCs due to gravity waves (e.g., Fueglistaler et al., 2003; Mann et al., 2005; Pierce et al., 2002). The application of mesoscale models, driven by reanalysis, has also been shown to be able to represent the impact of OGWs on the chemistry at specific regions on Earth (e.g., Carslaw et al., 1998; Eckermann et al., 2006; Noel & Pitts, 2012). As cirrus clouds have been found to play an important role in the climate system, implementations of fully interactive parameterizations of gravity-wave-induced formation of cirrus clouds is part of many chemistry-climate models (e.g., Barahona et al., 2014; Dean et al., 2007; Joos et al., 2008; Kärcher et al., 2019; M. Wang & Penner, 2010). However, the impacts of gravity-wave-induced temperature perturbations on atmospheric chemistry have seldom been examined in global stratospheric models. Weimer et al. (2021) used a local grid refinement approach with two-way interaction to simulate the global chemistry impact of a mountain wave event around the Antarctic Peninsula. Orr et al. (2020) parametrized orographic gravity-wave-induced temperature perturbations in the PSC scheme in the U.K. Unified Model and showed impacts on chlorine activation and the related ozone chemistry, considering the cold phase of the wave.

Here we present a method to account for the chemical impact of both the cold and warm phases of sub-grid scale OGWs on the global scale in a widely used community model. The method consists of derivation of temperature perturbation amplitudes from the gravity wave parameterization and its application to the chemistry. We briefly describe the model and the method in Section 2, and then evaluate the modeled temperature amplitudes $\hat{T}$ with COSMIC measurements and ERA5 reanalysis data in Section 3. We show examples of the calculated impacts of the gravity wave temperature effects on chemical concentrations in the stratosphere in Section 4, and finally discuss implications and future directions for this study in Section 5.

2. WACCM

The testbed for this study is the Specified Dynamics (SD) version of the Whole Atmosphere component (WACCM6) of the Community Earth System Model (CESM2.1) (Danabasoglu et al., 2020; Gettelman et al., 2019). Specified dynamics with a relaxation time of 50 hr are used in order to readily compare chemical impacts of single runs with and without the effects of the gravity waves, which could be difficult to separate from other sources of dynamical variability in free-running simulations. Here, the model is relaxed to the Modern-Era Retrospective Analysis for Research and Applications version 2 (MERRA2, Gelaro et al., 2017) using the FWSD component set (see Gettelman et al., 2019, for the definition). The relaxation is applied only between the surface and 1 hPa, which is why we restrict our analysis to this pressure range in this study. Horizontal discretization is done on a 1.25° × 0.9° longitude-latitude grid on 88 vertical levels up to about 140 km. The lower stratospheric vertical grid spacing is on the order of 1 km (e.g., Garcia et al., 2017). The physics time step is set to 30 min. This is also the standard time step used in the chemistry modules but here we examine the need for shorter time steps to capture gravity wave impacts on chemistry, see below for discussion of chemistry time stepping in this study. Detailed chemistry for the troposphere, stratosphere, mesosphere and lower thermosphere is calculated in Whole Atmosphere Community Climate Model (WACCM) (Emmons et al., 2020; Kinnison et al., 2007), including heterogeneous processes on tropospheric and stratospheric particles and clouds (e.g., Solomon et al., 2015; Wegner et al., 2013). Stratospheric ice in WACCM is calculated like ice clouds in the troposphere using the WACCM microphysics. The formation of super-cooled ternary solution droplets (STS) is based on the thermodynamic equilibrium between HNO_3, H_2SO_4 and water using the scheme described by Tabazadeh et al. (1994). The formation of nitric acid trihydrate (NAT) is also based on thermodynamic equilibrium using the equations by Hanson and Mauersberger (1988). Therefore, heterogeneous nucleation of STS and NAT particles is assumed in the model. Co-existence of STS and NAT is accounted for using a constant fraction for gaseous HNO_3 available for STS and NAT below the STS formation temperature (Wegner et al., 2013). For the sedimentation of NAT particles, responsible for denitrification of the stratosphere, a simple upwind scheme is applied in the model (Considine et al., 2000). The number densities of STS and NAT are fixed to $N_{\mathrm{STS}} = 10\ \mathrm{cm}^{-3}$ and $N_{\mathrm{NAT}} = 10^{-2}\ \mathrm{cm}^{-3}$, that is, larger amounts of the gaseous species available for STS and NAT lead to increased radii of the NAT particles and an increased surface area density (SAD) in the grid box.

The OGW parameterization of WACCM consists of source specification and wave propagation. The propagation and saturation assumes two dimensional steady-state hydrostatic waves as was done by McFarlane (1987) for OGWs. It is a column-based scheme that includes many simplifications, such as assuming purely vertical propagation of the wave and simplifications in the specification of the wave amplitudes. A detailed description of the OGW scheme in WACCM can be found in Appendix A. We use the displacement amplitude $\hat{\delta}$ (see Equation A10 in Appendix A) to calculate the temperature amplitude of the subgrid-scale gravity wave at each model grid point

$$\left|\hat{T}\right| = \hat{\delta}\frac{\partial\overline{\theta}}{\partial z}\frac{\overline{T}}{\overline{\theta}} \tag{2}$$

where $\overline{\theta}$ and $\overline{T}$ stand for the grid-scale potential temperature and air temperature, respectively, and z is the geometric altitude. The relationship between parameterized waves and the temperature evolution of an air parcel traveling through the wave field is not straightforward. For real-world (non-sinusoidal) obstacles the wave field and hence the air-parcel temperature evolution will depend on the shape of the obstacle as well as on features of the low-level flow such as blocking or flow diversion (Smith & Kruse, 2017, 2018).

In this study we make a simplifying assumption that the subgrid and sub-timestep temperature variation experienced by an air-parcel can be modeled as a sine wave:

$$T'\left(\xi', z, t'\right) = \hat{T}(z)\sin\left(k_{\mathrm{h}}\left[\xi' - \overline{U}t'\right] + \int^{z} m(\zeta)\mathrm{d}\zeta\right) \tag{3}$$

where we also assume the simple relation $k_{\mathrm{h}} = 1/\mathcal{W}_r$ and m is the vertical wave number. Here $\hat{T}(z)$ is the temperature perturbation amplitude diagnosed by Equation 2, $\mathcal{W}_r$ is the obstacle width diagnosed by the Ridge Finding

10.1029/2022MS003505

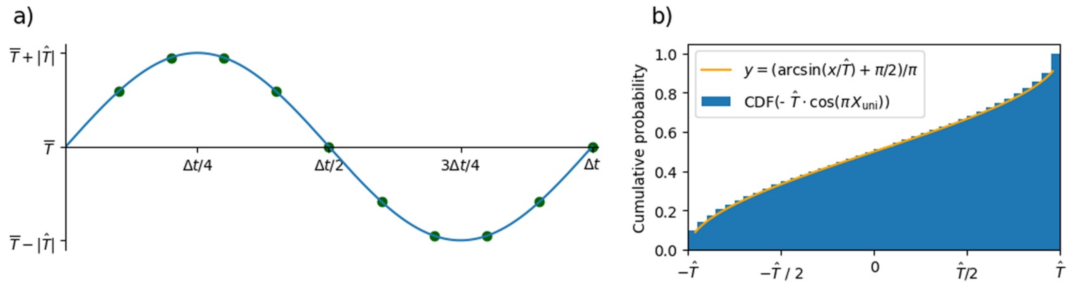

Figure 1. Illustration of (a) the temperature evolution in the sub-stepping approach using temporal sub-stepping (green dots) and (b) the stochastic approach using a sine-wave-distributed random T'.

Algorithm (RFA) described in Appendix B, and $\overline{U}$ is the horizontal wind component perpendicular to ridge/wavefront. The subgrid horizontal distance parallel to $\overline{U}$ is denoted by ξ' and the sub-stepped time is denoted by t'.

We simulate the influence of the wave-driven temperature perturbations in two ways, by temporal sub-stepping and stochastically. An air parcel influenced by OGWs will pass through the wave sequentially, that is, experiencing wave-like perturbations as illustrated in Figure 1a. This is why we applied the sub-stepping method as follows: we use the absolute value of $\hat{T}$ from Equation 2 at each model grid point as the amplitude of a sine wave and change the temperature within the chemistry by sampling the wave at 10 intermediate timesteps as depicted by the green dots in Figure 1a, with a corresponding reduction of the chemistry time step to 3 min compared to the standard timestep of 30 min in this model. The chemistry and all relevant processes (calculations of PSCs, tropospheric aerosols, reaction rate constants, photolysis rates, washout rates, chemistry solvers and settling of NAT particles) are updated during each 3-min substep. This method has the advantage of ensuring consistent evolution of multiple chemical species that may be interdependent in the same manner that an air parcel moving through the grid box would experience the effect of the wave. The sub-stepping approach assumes that all phases of the gravity wave temperature perturbations are sampled within one 30-min model time step. Assuming parcels are exposed to one wave cycle every 30 min is equivalent to assuming the wave intrinsic period (ν) is 30 min. Using the OGW dispersion relation $\lambda/\nu = \overline{U}$, this would be strictly accurate for mesoscale gravity waves of order $\lambda = 100$ km only in conditions of strong winds order 50 m s^{-1}, but is reasonable for polar vortex conditions.

However, sub-stepping through the chemistry on 3 min timesteps while the dynamics and dynamical-chemical coupling is calculated using the physics timestep of 30 min increases the overall model computation time by a factor of two and appears to lead to some artifacts in the chemical tracers at around 1 hPa, see Section 4. We also consider an alternative stochastic approach using sine-wave-distributed random T' without any sub-stepping. In this approach, T' is computed from a uniformly distributed random variable X_{uni} between 0 and 1 by

$$T'_{\mathrm{stoch}}(\vec{r}, t) = -\hat{T}(\vec{r}, t) \cdot \cos(\pi\, X_{\mathrm{uni}}), \quad X_{\mathrm{uni}} \in [0, 1) \tag{4}$$

which is shown in Figure 1b.

OGW events usually last longer than 1 day with similar amplitude (e.g., S. P. Alexander et al., 2009; Noel & Pitts, 2012). In addition, the phase of OGWs is generally fixed in space so that the temperature perturbations can exist over a specific area over a longer period. This means that the wave of Figure 1a is sampled at 48 stochastically chosen phases per day when using a physics time step of 30 min, so that the overall response of the chemistry to the temperature perturbation could be similar in long-term averages, although differences can be expected when looking at single time steps. Holding stochastically chosen T' for 30 min at a time is equivalent to assuming that the intrinsic period of the wave $\nu \gg 30$ min, 2–3 hr or more. This case would be more strictly true for the $\lambda = 100$ km gravity wave in slower wind conditions ∼9–13 m s^{-1}.

Another approach to decrease the overall computation time could be to apply the sub-stepping approach and sample the wave at fewer points than shown in Figure 1a. Sensitivity simulations decreasing the number of sub-steps showed systematic differences compared to ten-fold sub-stepping in the chemistry response. A number of sub-steps larger than 10 was found to lead to no large differences compared to ten-fold. Therefore, we restrict the analysis in this study to ten-fold sub-stepping, as shown in Figure S1 in Supporting Information S1.

Table 1
Simulations in This Study

Name	Remark
REF	Reference simulation without $\hat{T}$ parameterization
Sub-stepping (scaled)	Simulation with $\hat{T}$ scaled as discussed in Section 3
Sub-stepping (non-scaled)	Simulation with non-scaled $\hat{T}$
Stochastic (scaled)	Simulation using sine-wave-distributed random $\hat{T}$, scaled as discussed in Section 3

The steps to implement the sub-stepping approach in the model consist of: (a) adding Equation 2 to the model, (b) looping through the chemistry routines with reduced chemistry time step and temperature perturbations added to the model's grid-box mean temperature using Equation 3. For the stochastic approach, the second step consists simply of adding Equation 4 to the model's grid-box mean temperature without sub-stepping.

We performed simulations with and without the $\hat{T}$ parameterization, see Table 1 and Section 3 below regarding scaling. We chose the period 2007 to 2008 for the simulations presented here because it has the best coverage of the COSMIC measurements we use for comparison, see Section 3 and Appendix C. Daily maximum and averages as well as monthly averages are provided as output to investigate the chemical impact of the new parameterization. As an example, Figure 2 shows the global distribution of the 2-year maximum $\hat{T}$ at 15 hPa in WACCM. Since the method is applied to OGWs in this study, $\hat{T}$ is largest in the mountainous regions on the globe. The hot spots of OGWs show increased $\hat{T}$ values, for example, over the Antarctic Peninsula, the Andes and New Zealand in the Southern Hemisphere as well as Scandinavia, Greenland, the Ural Mountains, the European Alps, Apennines, the Carpathians and the Rocky Mountains in the Northern Hemisphere, where the impact on the chemistry in the stratosphere can be investigated with the new parameterization which was not possible before. Lower-level wind speeds vary seasonally in the model, leading to associated seasonal gravity wave temperature amplitudes (e.g., Hoffmann et al., 2013) which will be briefly discussed in Section 3.

There are numerous limitations of the OGW parameterization of WACCM that could affect calculated $\hat{T}$ (e.g., no lateral propagation, no dispersion, no wave-wave interaction, no damping other than that due to breaking). Because of these limitations and an expected overestimation of temperature amplitudes at higher altitudes, we seek to compare our estimated $\hat{T}$ values against other data sets, which is the subject of the next section.

3. Scaling of the New $\hat{T}$ Parameterization by Means of ERA5 and COSMIC

Since WACCM $\hat{T}$ is calculated globally, we focus on data sets that provide global coverage with high vertical resolution and discuss methods to compare WACCM $\hat{T}$ globally with these data sets. Satellite-based radio occultation

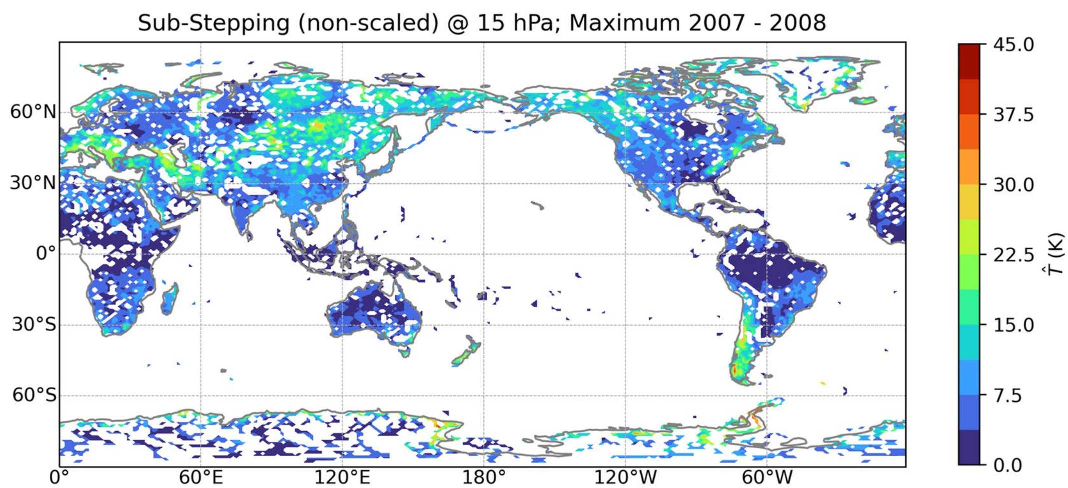

Figure 2. Two-year maximum $\hat{T}$ at 15 hPa as simulated by Whole Atmosphere Community Climate Model.

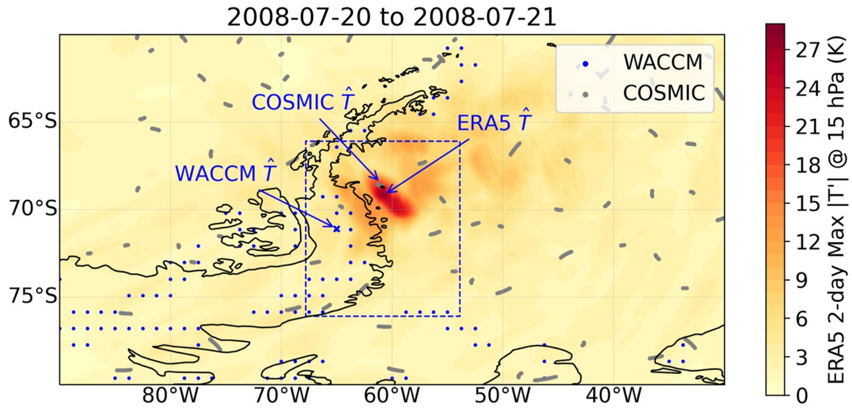

Figure 3. Illustration of the different coverage of each data set: blue points are Whole Atmosphere Community Climate Model (WACCM) grid points with $\hat{T} > 4$ K anywhere in the column where Constellation Observing System for Meteorology Ionosphere and Climate/Formosa Satellite 3 (COSMIC) and ECMWF Reanalysis version 5 (ERA5) are reliable, COSMIC profiles between 14 and 34 km are shown by the gray lines and ERA5 is in filled contours. The example shown is for a 2-day period, for details see text. The blue dashed region is used for best estimates of $\hat{T}$ for all data sets.

measurements as well as recent reanalysis data have been shown to satisfy these requirements (Dörnbrack, 2021; L. Wang & Alexander, 2010). We therefore use COSMIC and ERA5. Details about COSMIC, ERA5, and the methods to extract the gravity wave temperature perturbations are described in Appendix C. Both ERA5 and COSMIC will underestimate amplitudes of gravity waves with short wavelengths. COSMIC is generally only sensitive to $\lambda > 200$ km except in conditions of fortuitous alignment of the satellite line-of-sight (LOS) with the wave's lines of constant phase (M. J. Alexander, 2015; Schmidt et al., 2016). ERA5 will also damp OGWs with wavelengths smaller than about 150 km due to limited resolution, and previous studies show effects of the ECMWF model system resolution on OGW temperature amplitudes (Hoffmann et al., 2017; Kruse et al., 2022; Polichtchouk et al., 2022). In addition, gravity waves in ERA5 are damped starting at 10 hPa which might reduce the ERA5 gravity wave amplitudes at pressures larger than 5 hPa to some degree, too, but it has been shown that OGWs are well-resolved by ERA5 up to 1 hPa compared to lidar measurements (Ehard et al., 2018), see also Appendix C for some discussion about this.

There are fundamental differences between measurements by COSMIC, the ERA5 reanalysis, and coverage of WACCM: As shown in Figure 2, WACCM $\hat{T}$ is only significant over the mountains, that is, over land. Lateral propagation of gravity waves from one grid point to another cannot be simulated in WACCM because the parameterization operates in column physics. In reality, OGWs propagate not only vertically but also horizontally so that wave signals in COSMIC and ERA5 will often occur in the lee of mountains instead of only over the mountain. In addition, COSMIC provides measurements at irregularly distributed locations whereas ERA5 outputs hourly global coverage. This is illustrated in Figure 3 where COSMIC profiles during a 2-day period around the Antarctic Peninsula are denoted by gray points, the WACCM grid points with a $\hat{T}$ are depicted by blue dots, and ERA5 is in filled contours. Finally, COSMIC and ERA5 data are instantaneous temperature perturbations $T'\left(\vec{r}_0, t_0\right)$ whereas we decided to output daily statistics of the temperature amplitude $\hat{T}$ in WACCM, cf. Equation 3. As indicated by Figure 1 and Equation 3, the wave amplitude is the maximum temperature perturbation:

$$\hat{T} = \max\left|T'\right| \tag{5}$$

Therefore, we compare WACCM $\hat{T}$ with COSMIC and ERA5 on a global scale as described below.

The goal is to find the values in COSMIC and ERA5 that most likely correspond to the temperature amplitudes $\hat{T}$ in WACCM. The maximum T' for COSMIC and ERA5 is searched for in a region around the WACCM columns where non-zero $\hat{T}$ values are calculated. Since horizontal coverage is crucial for this procedure to ensure a COSMIC profile to be at the location of the maximum, only the WACCM columns are used where at least five COSMIC profiles are included in the regions, similar to the analysis by S. P. Alexander et al. (2009). Further, the temporal maximum of T' (ERA5 and COSMIC) and $\hat{T}$ (WACCM) is taken over n days where we will show a sensitivity study with $2 < n < 7$ which corresponds to the usual length of gravity wave events (e.g., S. P. Alexander et al., 2009; Noel & Pitts, 2012). An example for $n = 2$ is shown in Figures 3–5.

Since $\hat{T}$ is the amplitude of a sine wave, this should capture the impact of observed gravity waves in the data, cf. Figure 1. In Section 4, it will be shown that WACCM $\hat{T} > 4$ K can be connected to specific gravity wave events reported by the literature, see Figure 8. Therefore, we use the WACCM columns with $\hat{T} > 4$ K anywhere in the altitude range between 14 and 34 km where both COSMIC and ERA5 are reliable, see Appendix C. In order to account for the horizontal propagation of the gravity waves, the zonal extension of the region around the WACCM columns is set to half of the largest scale gravity wave resolved in the ERA5 perturbations (i.e., 500 km, see Appendix C) shifted by 400 km toward the lee of the mountain. The shift of 400 km downstream is derived from the typical horizontal scale of mountains in the order of $L = 100$ km (e.g., Bacmeister et al., 1994) so that effects directly above the mountain can also be accounted for. In the meridional direction, the region extends to ±5° around the WACCM grid point. An example of one region is illustrated by the white dashed lines in Figure 3. This is done all over the globe, which can be seen in Figure 4 for the same 2-day period as shown in Figure 3.

Altitude-dependent probability density functions of $\hat{T}$ in 4-km height bins are calculated for all the data sets, see the example in Figure 5 for the height bin of 22–26 km. As might be expected due to the limitations of the parameterization, WACCM overestimates the large $\hat{T}$ values and underestimates low $\hat{T}$ values compared to both COSMIC and ERA5 (left column of Figure 5). This is shown by a larger probability density of WACCM $\hat{T}$ for $\hat{T} > 5$ K. Influence of nonorographic gravity waves, although being minimized by the described approach, could partly explain this underestimation (e.g., Bacmeister et al., 1999), but we expect their effect to be small because we use the 4-dimensional maximum amplitude in the neighborhood of OGW activity in WACCM. Scaling factors between 0.1 and 10 applied to the WACCM $\hat{T}$ values are tested and the scaling factor minimizing the differences between the probability density functions of WACCM and the respective data set is used to derive the scaling profile, described below. The right column of Figure 5 shows the WACCM $\hat{T}$ distribution together with the data set's distribution. By applying a scaling factor of 0.6 to $\hat{T}$ in the example altitude bin of Figure 5, the number of grid points in WACCM with smaller $\hat{T}$ increases accordingly.

As mentioned above, these scaling factors are calculated for each 4-km altitude bin and for varying the number of days to collect the maximum between 2 and 7. The resulting distributions of scaling factors for each altitude bin are shown in Figure 6, together with the average of the medians of COSMIC and ERA5. The stratospheric scaling factors vary between 0.6 and 0.8 and increase toward 1 at lower altitudes. In the real world, waves are not monochromatic, so wavepackets can disperse (and thus reduce local amplitude) and they can also propagate laterally as already shown, whereas in WACCM the waves are confined to a column in which they grow exponentially until they break. These limitations will become more and more relevant with increasing altitude, thus leading to the need to scale down the WACCM values more at higher altitude in order to bring the model into agreement with COSMIC. Hence, temperature amplitudes are probably overestimated by WACCM but underestimated by the data sets, as mentioned above, which is why we will show results of simulations using the scaling profile of Figure 6 and unscaled results, see also Table 1.

Due to the seasonal cycle of surface wind and thus gravity wave activity (Hoffmann et al., 2013), $\hat{T}$ also shows a seasonal cycle with largest values during local winter. Results of the monthly and zonal maximum $\hat{T}$ for the two WACCM simulations and ERA5 are shown in Figure 7 for January and July 2008, that is, 1 month in the respective winter seasons in each hemisphere. The gap in WACCM $\hat{T}$ at around 60°S can be explained by the fact that there are no mountains at this latitude generating gravity waves. Note that unlike the OGW parameterization in WACCM, OGWs can propagate horizontally, so they can propagate into the Drake Passage. In addition, nonorographic gravity waves are generated and propagated in this region (Hendricks et al., 2014). Therefore, there is no corresponding gap in ERA5.

The $\hat{T}$ values increase with altitude. They reach values as high as 70 K in the non-scaled simulation, which has not been reported in measurements to date. Kaifler et al. (2020) found upper stratospheric $\hat{T}$ values up to about 40 K above the Andes during an event in 2018. The scaling applied to $\hat{T}$ reduces these large values to the range observed by Kaifler et al. (2020). Figure 7 illustrates that the $\hat{T}$ values are comparable to ERA5 in the pressure range between 5 and 20 hPa when the scaling profile is applied there. Thus, the scaled $\hat{T}$ values in WACCM are broadly consistent with this data set in the stratosphere, and we will investigate illustrative impacts of both the scaled and unscaled $\hat{T}$ in this new parameterization on the stratospheric chemistry in the next section.

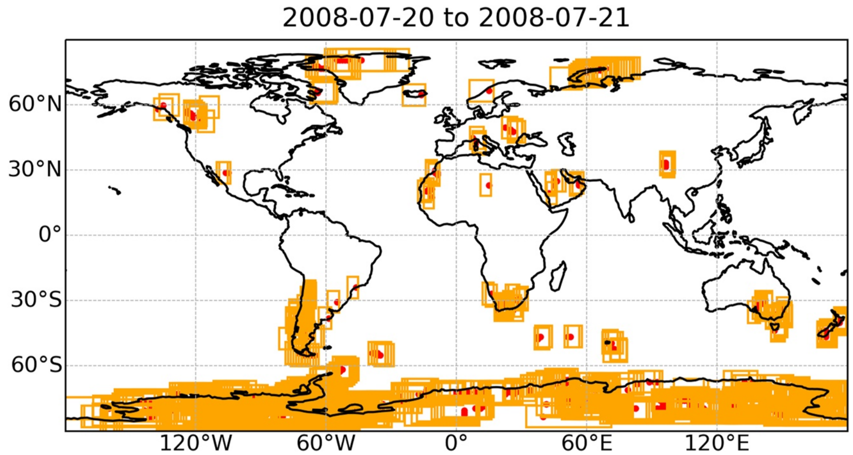

Figure 4. Illustration of the regions over the globe where significant orographic gravity wave (OGW) forcing occurs in Whole Atmosphere Community Climate Model (WACCM) (orange) and the corresponding grid points (red) during 20–21 July 2008.

4. Impacts on the Stratospheric Chemistry

This section discusses the impact of applying the new $\hat{T}$ parameterization to the chemistry in WACCM. We focus the analysis of the influence in the stratosphere. We first show some timeseries of the relevant species at two OGW hot spots (Section 4.1). This is followed by an examination of the influence at all known hot spots of OGWs on the globe in Section 4.2. After that, we investigate the effect of the new parameterization on the zonal mean distributions of PSCs (Section 4.3), chlorine activation (Section 4.4), nitrogen species (Section 4.5) and ozone (Section 4.6).

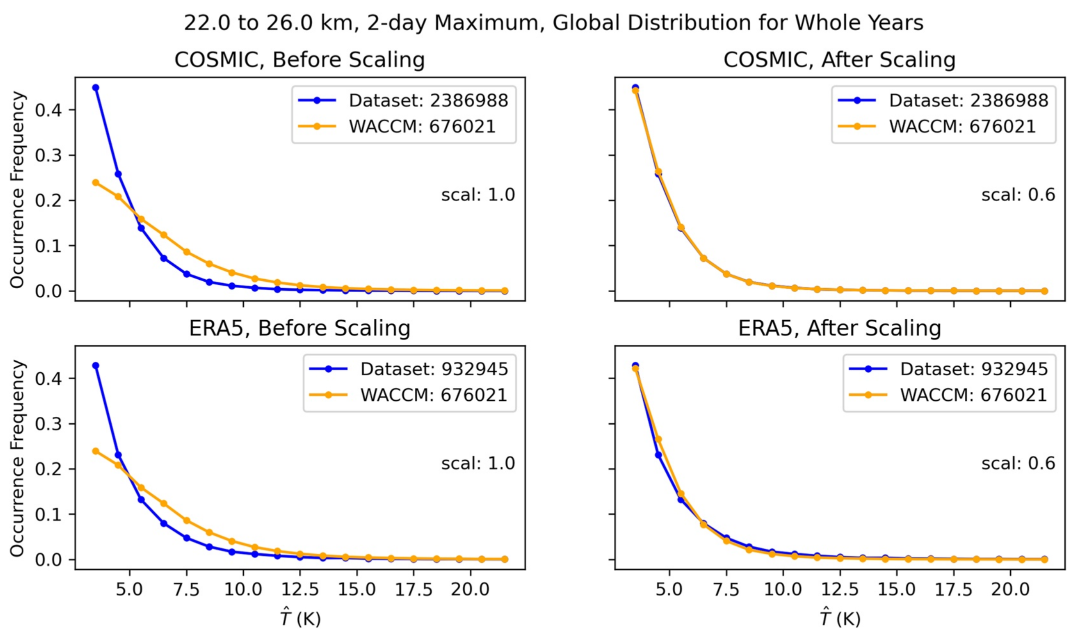

Figure 5. Probability density functions of $\hat{T}$ for Whole Atmosphere Community Climate Model (WACCM) (orange) and the respective data set (blue) in the 4-km altitude bin 22–26 km and the scaling factors that minimize the differences between the probability density functions. By applying a scaling factor of 0.6 to $\hat{T}$, the number of grid points in WACCM with lower $\hat{T}$ decreases.

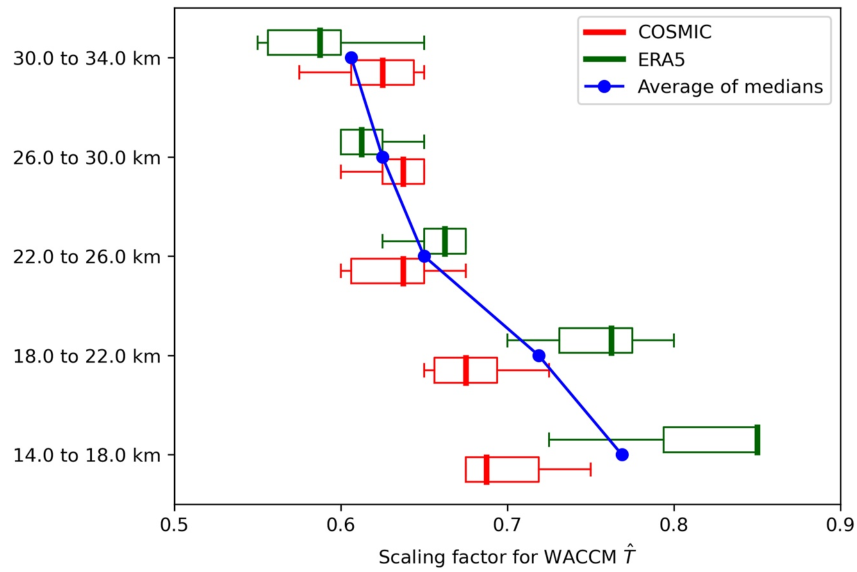

Figure 6. Altitude-dependent distributions of scaling factors using the method illustrated in Figures 3–5 by varying the periods from 2 to 7 days to get max $\hat{T}$ for all data sets. The "scaled" experiments use this scaling profile for Whole Atmosphere Community Climate Model (WACCM) $\hat{T}$ with no scaling (scaling factor 1) at lower altitudes and a constant scaling factor above 34 km. The "non-scaled" experiment uses a scaling factor of 1 at all altitudes.

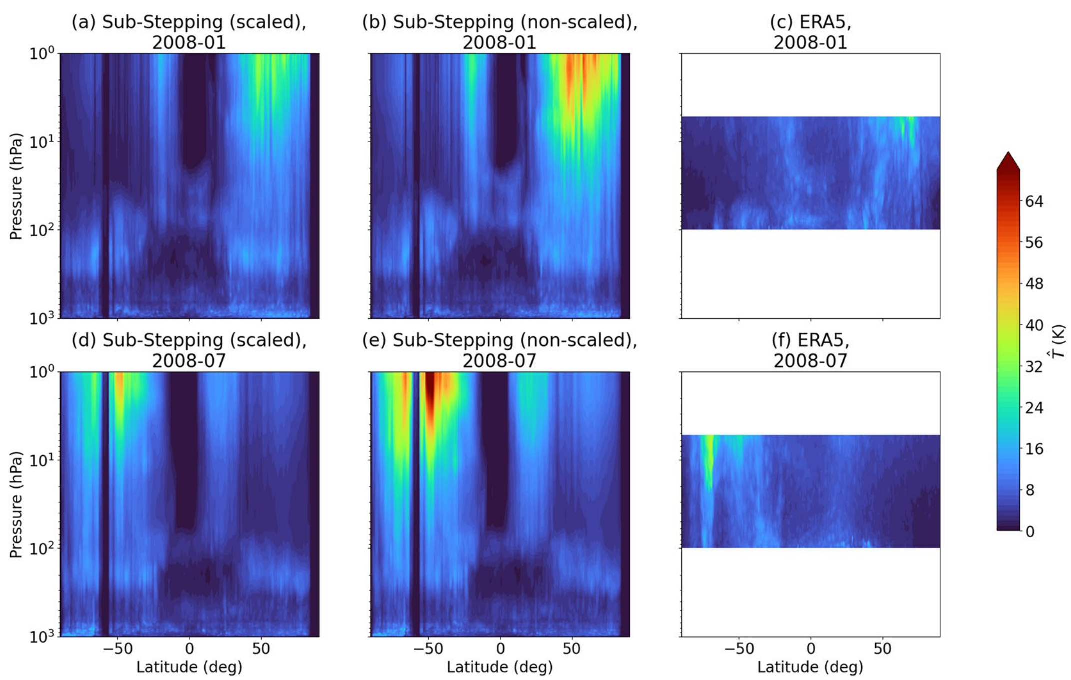

Figure 7. Zonal monthly maximum $\hat{T}$ in January (first row) and July 2008 (second row) for the (a, d) "Sub-stepping (scaled)" and (b, e) "Sub-stepping (non-scaled)" Whole Atmosphere Community Climate Model (WACCM) simulations and (c, f) ECMWF Reanalysis version 5 (ERA5). $\hat{T}$ in "Stochastic (scaled)" is the same as in "Sub-stepping (scaled)." For $p < 1$ hPa, the nudging of WACCM toward Modern-Era Retrospective Analysis for Research and Applications version 2 (MERRA2) decreases with no nudging for $p < 0.3$ hPa, which is why the analysis in this study is restricted to lower altitudes, see also Section 2.

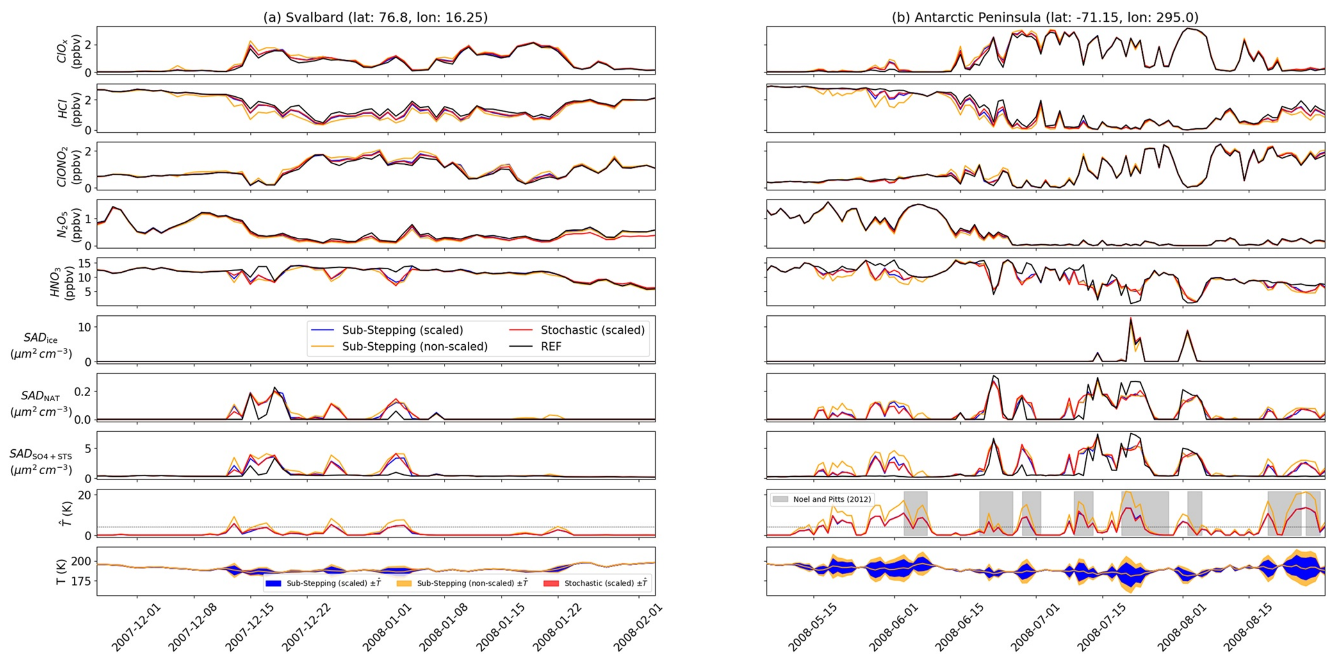

Figure 8. Timeseries of daily mean concentrations of different trace gases and aerosols at single Whole Atmosphere Community Climate Model grid points over (a) Svalbard and (b) the Antarctic Peninsula at 15 hPa. The lines correspond to the simulations of Table 1. The first five rows show the volume mixing ratios of ClO_x, HCl, $ClONO_2$, N_2O_5, and HNO_3. The next three rows consist of timeseries of the surface area density (SAD) of the three polar stratospheric cloud types: ice, nitric acid trihydrate (NAT) and super-cooled ternary solution (STS). The last two rows show $\hat{T}$ and T. The gray shaded regions in the timeseries over the Antarctic Peninsula are gravity wave events as reported by Noel and Pitts (2012). The dashed line in the $\hat{T}$ timeseries (second from bottom row) shows the threshold of 4 K to distinguish orographic gravity wave (OGW) events from the background used for the scaling, see Section 3. The colored ranges in the lowest row shows $\pm\hat{T}$ around the mean grid-box temperature in the model for the different simulations.

4.1. Timeseries at OGW Hot Spots in Both Hemispheres

As a first example, Figure 8 shows timeseries of the daily mean values of various variables at 15 hPa over two hot spots of OGWs: Svalbard (left column) in the Northern Hemisphere and the Antarctic Peninsula (right column) in the Southern Hemisphere (e.g., Dörnbrack et al., 2017; Noel & Pitts, 2012). Orange, blue, red and black lines in all panels correspond to the "Sub-stepping (non-scaled)," "Sub-stepping (scaled)," "Stochastic (scaled)" and "REF" simulations, respectively.

The two rows at the bottom of Figure 8 show WACCM $\hat{T}$ and the absolute temperature with $\pm\hat{T}$ as colored shading and lines, respectively. Time intervals with substantial $\hat{T}$ values are simulated at both hot spots. In the case of the Antarctic Peninsula, the gray shaded time periods also indicate when gravity wave events were obtained in the mesoscale simulation by Noel and Pitts (2012). These simulations were setup using the Weather Research and Forecasting Model in a region of $1{,}800 \times 1{,}800\ km^2$ around the Antarctic Peninsula with a horizontal grid spacing of about 20 km, with lateral boundary data from reanalysis data. Noel and Pitts (2012) performed simulations of several winters including the austral winter 2008 where they provided the days with higher OGW activity, shown in Figure 8. The good general agreement for the time periods with $\hat{T} > 4$ K (black dashed lines in the panel) with Noel and Pitts (2012) bolsters confidence in our findings on corresponding chemical impacts, and is why we are using this threshold for comparison with the data sets in Section 3. Note that the simulation by Noel and Pitts (2012) started on 01 June 2008. The comparison with Noel and Pitts (2012) demonstrates that the new parameterization is able to represent specific mountain wave events and their intermittent character (e.g., Hertzog et al., 2012).

These temperature perturbations have impacts on several aspects of the chemistry in WACCM. The rows 6–8 of Figure 8 show the timeseries of ice, NAT and STS SADs for the four model cases. During periods with increased $\hat{T}$, there is also an increase of STS and NAT SADs. As the number densities of NAT and STS are fixed, the SAD is an indicator of the radius of these particles. Especially at the start of the winter in May 2008 for the Antarctic Peninsula, the large-scale temperature is often too high to form NAT, STS and ice, but with $\hat{T}$ applied they are formed, indicated by an increased SAD of these particles during that time. This is consistent with previous studies which found that mountain-wave-induced PSCs are most important at the start of the polar winter (e.g., McDonald et al., 2009). Due to the increased radii of NAT particles we also see enhanced denitrification of the stratosphere in the simulations with $\hat{T}$ applied (not shown).

The change in PSC SAD and denitrification as well as the direct temperature change and associated reactivity changes due to $\hat{T}$ then lead to changes in the chlorine and nitrogen compounds in the model, which are sometimes substantial (rows 1 to 5). Gaseous nitric acid (HNO_3, fifth row) is taken up by the aerosols and therefore decreases with the additional appearance of STS and NAT due to $\hat{T}$. N_2O_5 (fourth row) reacts on the surface of PSCs and is hence depleted during the events as a result of the $\hat{T}$ parameterization. The reactive chlorine species, summarized as ClO_x (first row) with

$$\mathrm{ClO}_x = \mathrm{Cl} + \mathrm{ClO} + \mathrm{HOCl} + 2\,\mathrm{Cl}_2 + 2\,\mathrm{Cl}_2\mathrm{O}_2 + \mathrm{OClO} \tag{6}$$

increase due to the increase in PSC SAD, whereas the reservoir species HCl (second row) is depleted as a consequence, which is known as chlorine activation (e.g., Solomon, 1999). HCl has a longer lifetime than the active chlorine species, which is why the changes are transported downstream of the mountain and persist longer than the gravity wave events themselves can be seen. The change in chlorine nitrate ($ClONO_2$, third row) depends on the availability of active chlorine and nitrogen. In both of these illustrative time series, $ClONO_2$ is increased as a result of $\hat{T}$, known as the "collar" formation (Solomon et al., 2016; Toon et al., 1989).

Although overall changes in the concentrations are relatively small, they can be locally as large as about 50% for some species and events. This highlights the importance of considering gravity wave processing in models that may seek to interpret airborne or other measurements. For example, attempts to infer the exact temperatures of chlorine activation processes based on field measurements may require consideration of gravity wave-driven perturbations. These are better simulated with the sub-stepping approach to ensure realistic simulation of nonlinear chemistry, since the large temperature fluctuations in successive time steps inherent in the stochastic approach can produce unrealistic transients in chemical composition on time scales comparable to the model's time step.

In summary, Figure 8 shows that the new parameterization is able to reproduce specific gravity wave events with direct impact on the aerosols and the associated chemistry in the model. As expected from the scaling factor applied, the chemistry response is larger for the "Sub-stepping (non-scaled)" simulation compared with the REF case. The stochastic method is able to reproduce the chemistry impact of "Sub-stepping (scaled)" in all the time series shown, with minor differences in its amplitude on specific days.

4.2. Local Influences at the OGW Hot Spots on the Globe

Chemistry impacts are not only restricted to Svalbard and the Antarctic Peninsula, but occur at all known hot spots of OGWs in the model. Figure 9 shows global maps of the 2-year maximum or minimum relative difference between "Sub-stepping (scaled)" and REF at 15 hPa for several species in the model. The largest relative differences are connected to the global hot spots of gravity waves, especially for HNO_3 (panel d and e): Svalbard, Iceland, Scandinavian Mountains, Ural Mountains, Andes, Antarctic Peninsula and the edge of the Transantarctic Mountains. Increased relative differences can also be seen around subtropical mountains such as the Himalayas, the Philippines and Madagascar. These mountain-wave-induced changes propagate downstream of the mountains, visible in the daily averaged results shown here. HCl (panel b) and $ClONO_2$ (panel c) have longer lifetimes than the active chlorine species so that the changes propagate further downstream, but there is still a connection to the noted hot spots of OGWs in their (negative) changes.

As mentioned above, HNO_3 (panel d and e) is taken up by PSCs but it is also produced by heterogeneous reactions on the surface of PSCs (Solomon, 1999). That is why the largest positive and negative changes in HNO_3 can be found directly above the mountains, where $\hat{T}$ is largest, cf. Figure 2, with maximum values locally larger than 350% and minimum relative differences down to −54%. Such substantial changes could confound interpretation of satellite or in-situ measurements of these species, if gravity wave-induced temperature perturbations are not fully taken into account. Indeed, on some days in the simulations, chlorine is activated as a result of the $\hat{T}$ parameterization whereas no active chlorine was obtained without it. This is manifested by local maximum relative differences in ClO_x that can exceed 2,000%.

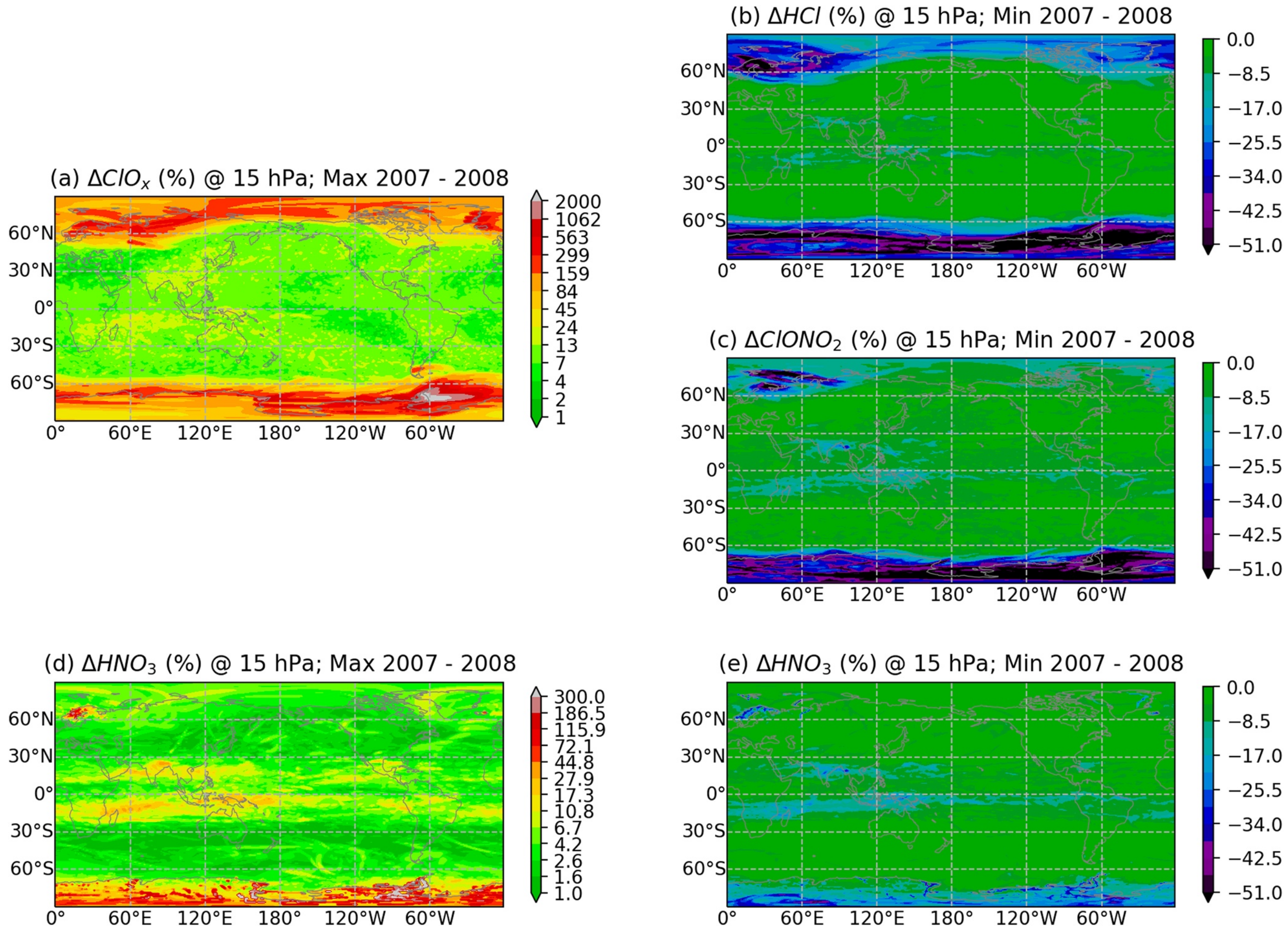

Figure 9. Two-year maximum (left column) and minimum (right column) relative difference between "Sub-stepping (scaled)" and "REF" simulations of daily averaged (a) ClO_x, (b) HCl, (c) $ClONO_2$ and (d, e) HNO_3 at 15 hPa.

4.3. Zonal Mean Effect on Polar Stratospheric Clouds

These large local changes are then transported downstream of the mountains and mixed with unperturbed air masses and lead to monthly mean changes. Figure 10 shows the zonal monthly mean differences in SAD of PSCs between the three $\hat{T}$ simulations and REF in January and July 2008. Both STS (third row) and NAT (second row) SADs show an increase in the polar region as a result of $\hat{T}$, which is expected from the non-linear growth of these particles at low temperatures (e.g., Carslaw et al., 1994). The tropopause height changes considerably during 1 month so that the altitude region close to the monthly zonal mean tropopause height (blue line in the figure) still may be misidentified do be tropospheric or stratospheric and may skew the monthly average shown in the figure. Ice (first row) concentrations are orders of magnitude larger in the troposphere than in the stratosphere. Therefore, the largest zonal mean differences relative to the control run occur at the tropopause. Zonal mean relative differences show larger increases at the edge of the polar vortex in both months, see Figure S2 in Supporting Information S1. Changes are also obtained in particle abundances (ice, NAT, and STS) near the tropical tropopause, where temperatures approach values as cold as the Antarctic vortex, particularly in the summer when monsoon heterogeneous chemistry can be significant (Solomon et al., 2016). This raises the potential for impacts on cirrus, and water vapor transport into the stratosphere, but these are beyond the scope of the present paper. The decrease of the STS SAD above the tropical tropopause in January 2008 can probably be explained by the lowest absolute temperatures combined with increased $\hat{T}$ values in this region where the warm phase of the OGW will significantly (and non-linearly) decrease the SAD of sulfates. In addition, the HNO_3 volume mixing ratio in the model is lower at the tropical

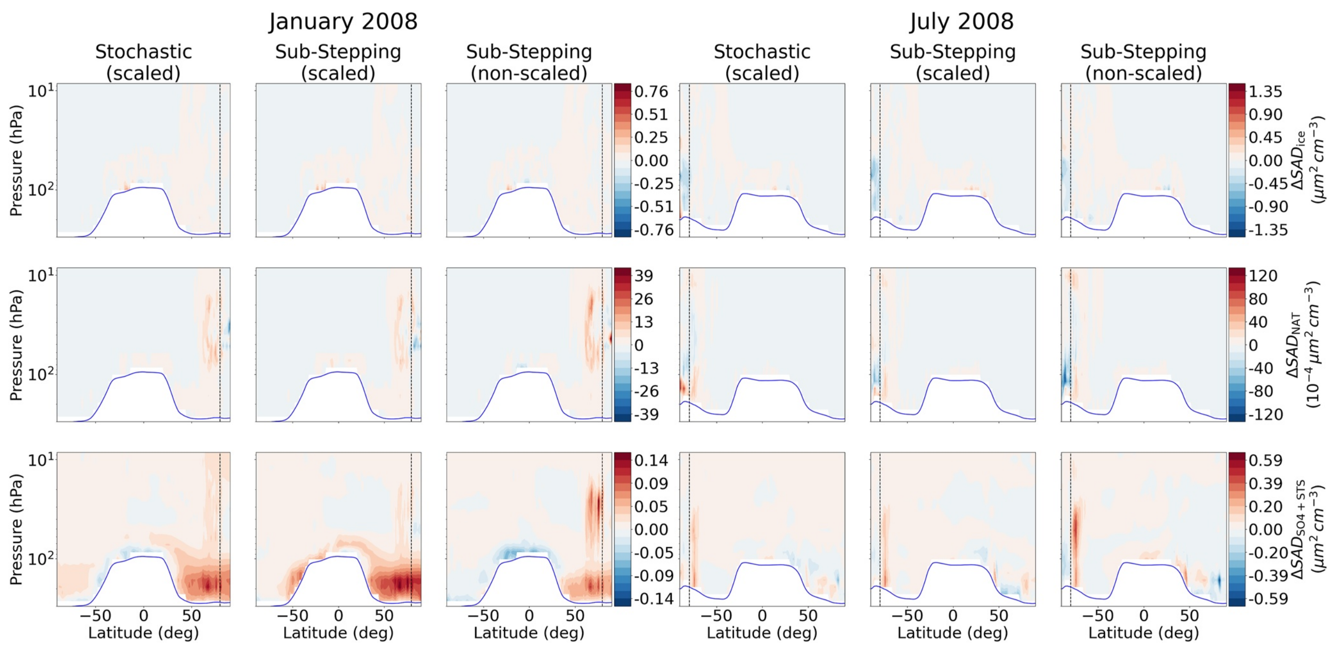

Figure 10. Zonal monthly mean difference between "Sub-stepping (scaled)" or "Sub-stepping (non-scaled)" and REF simulations in the stratosphere during January and July 2008 for ice (first row), nitric acid trihydrate (NAT) (second row) and super-cooled ternary solution (STS) (third row) surface area densities (SADs). The blue line shows the zonal mean tropopause height and the dashed black vertical line separates the polar night from the rest of the globe. Tropospheric values are masked; see text for explanation. Note the different color ranges for each month and variable.

tropopause region than in the polar winter, so that increases of the SAD due to lower temperature are not as large as in the polar regions (e.g., Carslaw et al., 1994, for the temperature and HNO_3 dependence of the SAD).

All species discussed in Section 4.2 also show changes in the troposphere. These occur with irregular patterns as soon as something is changed in the applied parameterizations. To test the reason for this, a simulation randomly perturbing the initial temperature of REF on the order of 10^{-14} K, as done in previous work with CESM (Kay et al., 2015; Shah et al., 2022; Stone et al., 2019), led to similar tropospheric changes of these species, see Figure S3 in Supporting Information S1 for ozone. Thus, these changes are apparently a result of dynamical changes, which originate from intermediate solutions at the smaller chemistry time step when applying the chemistry sub-stepping and which then change the trace gas concentrations in the model. Since some of these concentrations interact with radiation in the model, there is a feed back to the dynamical variables like temperature and pressure. Therefore, the troposphere is excluded from the analysis of this study. In the stratosphere, the mixing ratios of these species are larger and the time scales are longer than in the troposphere where they are partly determined by convective transport, so that these changes are relatively small in the stratosphere.

4.4. Zonal Mean Effect on Chlorine Species

The changes in aerosol SAD as well as the change in temperature itself due to $\hat{T}$ result in changes of many gas-phase species. Figure 11 shows the zonal monthly mean relative changes of the chlorine species for the same months in the winter high latitudes. As expected from the timeseries in Figure 8, both ClO_x and $ClONO_2$ are increased in the winter polar lower stratosphere whereas HCl is decreased. The changes are larger in the southern compared to the northern winter and depend on the scaling employed, which emphasizes that the changes are due to $\hat{T}$ and not to other processes in the model. In the "Sub-stepping (scaled)" simulation, zonal monthly mean relative differences as high as 30%, 50%, and −20% can be found for ClO_x, $ClONO_2$, and HCl, respectively, in these regions. This implies substantial gravity wave-driven impacts that could influence interpretation of local observations of those species, because measurement campaigns investigating the impact of OGWs are usually set up in the regions where largest differences occur in the simulations (e.g., Rapp et al., 2021; Taylor et al., 2019). In addition, it could impact regional comparisons to satellite measurements. The monthly and

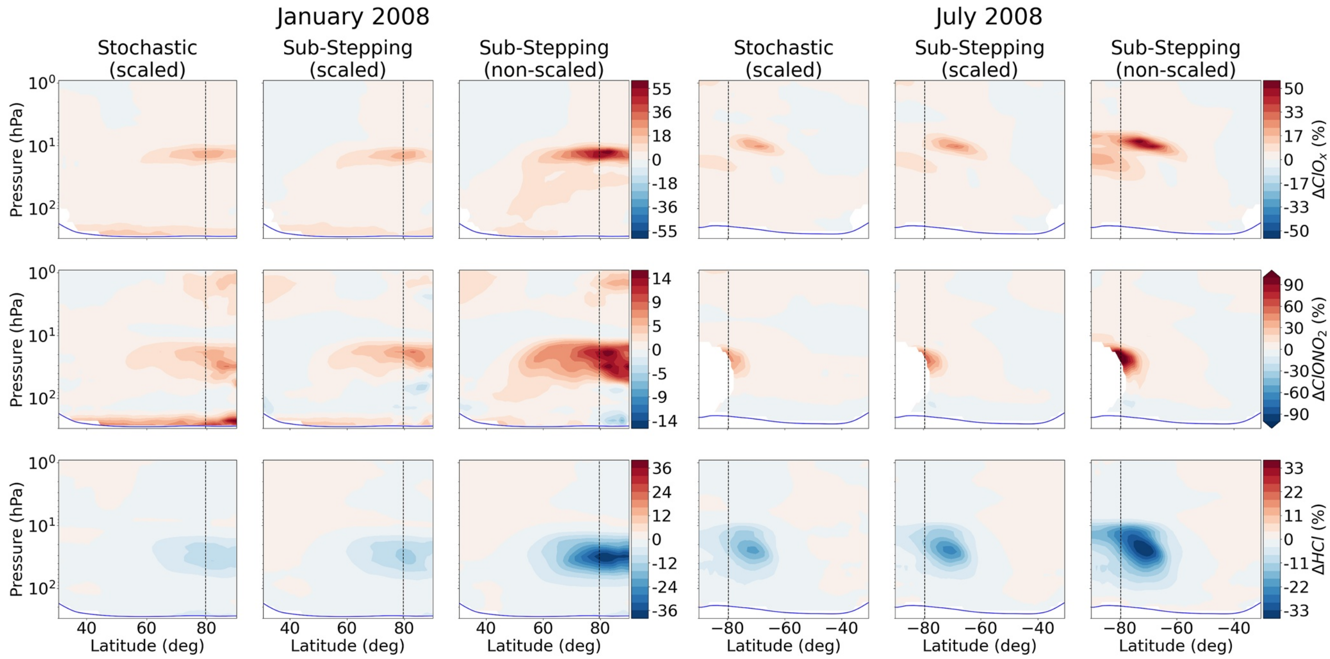

Figure 11. Zonal monthly mean relative differences (in %) of the volume mixing ratios for ClO_x (first row), $ClONO_2$ (second row) and HCl (third row) for the winter polar latitudes. Relative differences with absolute values lower than 1 pptv are removed from the analysis. Otherwise, same configuration as in Figure 10.

zonally averaged stratospheric response in terms of chlorine activation is similar for the stochastic approach compared to "Sub-stepping (scaled)."

Many of the stratospheric changes are located at the edge of the polar vortex where gradients are large and temperatures approach the thresholds of PSC chemistry, and hence display an increased sensitivity to temperature changes, consistent with previous observations of "NAT belts" along the vortex edge due to OGWs (e.g., Höpfner et al., 2006). This is shown by the curved shape of the changes, especially for ClO_x and southern winter $ClONO_2$ and HCl. Since the northern hemisphere polar vortex is unstable compared to the southern hemisphere vortex, the changes in the longer-lived (and therefore transported) $ClONO_2$ and HCl are not as confined in latitude as those in the southern hemisphere.

The comparison of the "Sub-stepping (scaled)" and "Sub-stepping (non-scaled)" experiments demonstrates the importance of a correct representation of gravity wave temperature perturbations in the chemistry of WACCM. Although $\hat{T}$ is only increased by about 60% the changes in ClO_x and HCl in the "Sub-stepping (non-scaled)" simulation are larger than the scaling factor in $\hat{T}$. This illustrates the non-linearity of the chemistry response on temperature changes.

4.5. Zonal Mean Effect on Nitrogen Species

Changes due to the gravity wave temperature perturbations can also be seen in the nitrogen-containing species, see Figure 12 for the zonal monthly mean relative differences of HNO_3 (first row), N_2O_5 (second row) and NO_x (third row), where

$$NO_x = N + NO + NO_2 \tag{7}$$

As already discussed, the impact of temperature on the chemistry of HNO_3 is two-fold, which is why the net effect in the lower stratosphere is small. In January 2008, the net relative differences near 30 hPa in the polar region are lower than 3%. In July, the increase due to the heterogeneous reactions slightly dominates the uptake with relative differences around 6% in the "Sub-stepping (non-scaled)" simulation. The increase of HNO_3 in the "Stochastic (scaled)" simulation at around 7 hPa in the respective winter also occurs in the other simulations, but is one order of magnitude smaller. This can be explained by an increased SAD of aerosols in this region. N_2O_5 reacts with water vapor on the surface of PSCs, which is why the largest negative changes in the lower stratosphere are

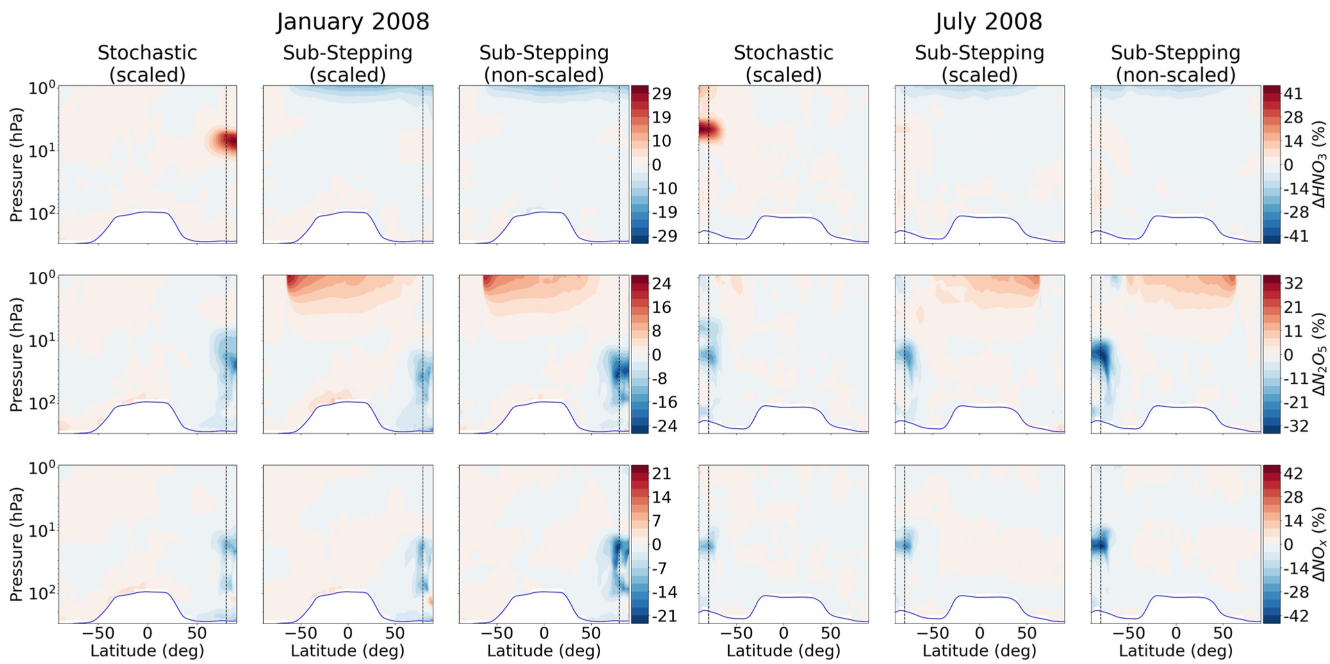

Figure 12. Zonal monthly mean relative differences (in %) of the volume mixing ratios for HNO_3 (first row), N_2O_5 (second row) and NO_x (third row). Otherwise, same configuration as Figure 10.

connected to the occurrence of PSCs and the chlorine chemistry, cf. Figures 10 and 11. NO_x is a by-product of the N_2O_5 chemistry so that the changes on the order of around −20% to −45% are correlated with N_2O_5.

Both HNO_3 and N_2O_5 in the "Sub-stepping (scaled)" and "Sub-stepping (non-scaled)" simulations show relative changes at around 1 hPa that do not change with the applied scaling factor. This effect can also be seen in species like OClO, HOCl, and ClO (not shown). By sensitivity simulations that change the number of chemistry sub-steps but not the temperature it was found that these relative differences are a result of the sub-stepping rather than a physical effect. These artifacts are therefore removed when using the stochastic approach, where no sub-stepping is applied.

4.6. Zonal Mean Effect on Ozone

A number of these species can in principle influence ozone, but we find that effects on ozone are quite small at least in the monthly average. The impact on ozone in terms of zonal monthly mean relative differences is illustrated in Figure 13. Generally, the impact on ozone is most prominent at the end of the polar ozone depletion season. Therefore, the relative changes for ozone are shown for March and October 2008. Since air masses subside in the polar vortex, the maximum lower stratospheric changes in ozone occur at lower altitudes than that of PSCs, chlorine and nitrogen species in the previous figures. At the end of the northern hemispheric winter, changes between −1% and −2% can be related to the gravity wave temperature perturbation. In the southern hemisphere during October, the changes are larger with −3% to −8% in the pressure range from about 100 to 30 hPa.

Monthly average negative changes in ozone occur all over the Antarctic Continent, as can be seen in terms of total column ozone in Figure 14 averaged over all simulated October months. The changes are on the order of −2 to −4 DU in the "Sub-stepping (scaled)" and "Sub-stepping (non-scaled)" simulations and less than −1 DU in the "Stochastic (scaled)" simulation. Orr et al. (2020) found larger changes with their approach to account the interaction between OGWs and PSCs using the UK-UMCA model. They obtained local changes for October 2000 up to ±7.5 DU. However, their simulation was free-running with boundary conditions from the year 2000 and these changes are a result of both chemistry and a horizontal shift of the polar vortex. Further, they applied the temperature change to PSCs only and the direct effect on the chemistry was missing. Perhaps most important, they accounted for the cold phase of the gravity wave only, while here we consider the full temporal evolution

10.1029/2022MS003505

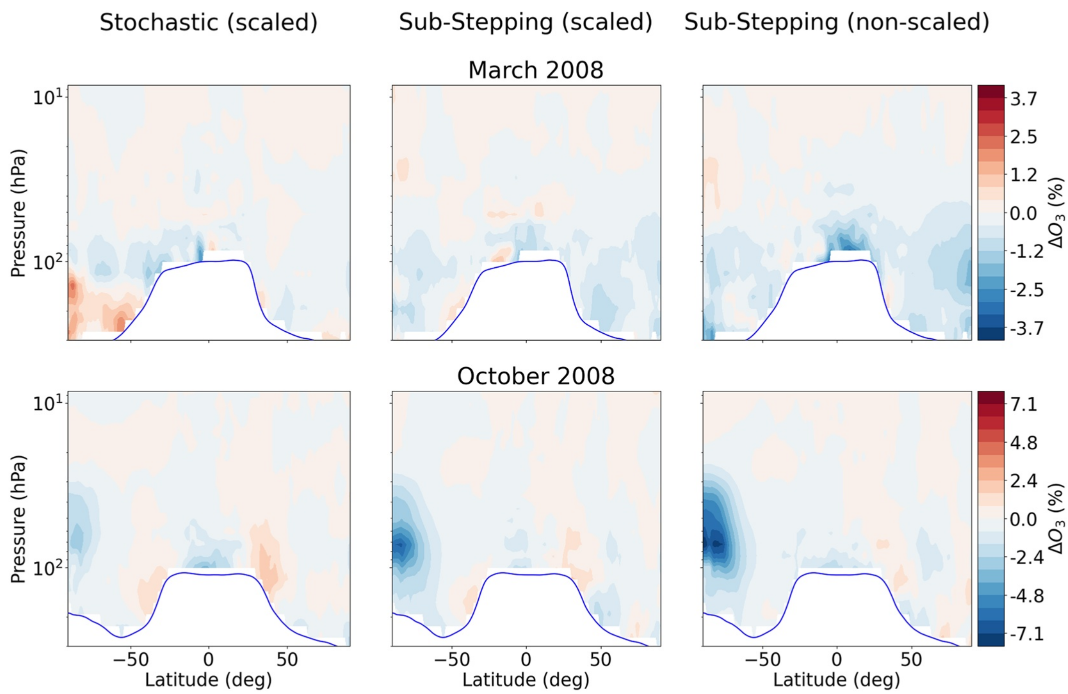

Figure 13. Same as Figure 11 but for O_3 in March and October 2008.

of the wave through its warm as well as cold phases, and the potential for cancellation between the two. The more nearly linear the chemistry is, the more complete the cancellation will be. On the other hand, nonlinear chemistry would be expected to yield a net effect. Hence, their simulations were a maximum estimate of the gravity wave effect.

In summary, we have shown in this section that the $\hat{T}$ parameterization leads to notable changes of the polar stratospheric chemistry at all known hot spots of OGWs on the globe. Gravity-wave-induced temperature changes lead to enhanced formation of aerosols and heterogeneous chemistry, resulting in increased chlorine activation and decreased polar ozone. Thus, this study enables the chemistry climate modeling community to account for this process interactively, consistent with the internal parameterizations and can be expected to yield more realistic interactions and better representation of the chemistry.

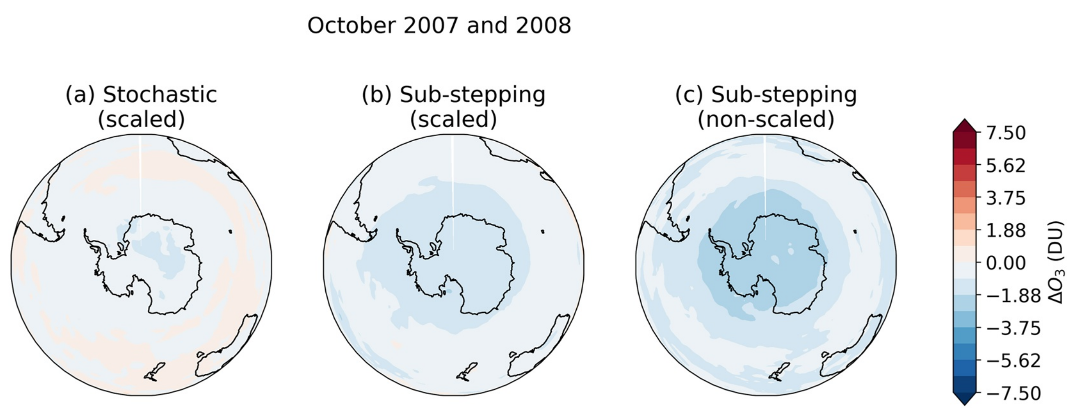

Figure 14. Average difference between (a) "Stochastic (scaled)," (b) "Sub-stepping (scaled)" or (c) "Sub-stepping (non-scaled)" and REF of total column ozone over the Antarctic Continent for October 2007 and 2008. Same color bar as by Orr et al. (2020).

10.1029/2022MS003505

5. Discussion and Conclusions

In this study, we developed a method to account for the effects of subgrid-scale OGW temperature perturbations on the chemistry at global scale, a missing piece in chemistry-climate models. The method uses the subgrid-scale gravity momentum flux and large-scale parameters like the wind speed and the vertical gradient of the potential temperature to calculate a temperature perturbation amplitude due to gravity waves. This amplitude is then applied either by a sub-stepping of the chemistry with a sine-wave perturbation of the grid-scale temperature or by sine-wave distributed random temperature perturbations.

The temperature amplitudes $\hat{T}$ were compared with COSMIC satellite radio occultation measurements and ERA5 reanalysis data, which are both suitable data sets for extracting information about gravity waves on a global scale. By comparing the $\hat{T}$ distributions of WACCM and the two data sets at altitudes between 14 and 34 km, we found that scaling factors between 1 and 0.6 depending upon altitude minimize the differences in the probability density distributions of the temperature perturbations. Since both COSMIC and ERA5 underestimate $\hat{T}$ for the shorter horizontal scale OGW, we tested effects of both scaled and unscaled WACCM sub-grid scale $\hat{T}$.

We presented various examples illustrating that the new parameterization leads to local as well as global changes in the model chemistry, many of which can be explained by the non-linear temperature dependence of both the formation of aerosols and associated heterogeneous chemistry and the gas-phase chemistry. Some of these changes can be locally very large (much more than 100%), which could influence interpretation of satellite or in-situ measurements, depending on their temporal and spatial sampling. The parameterization is able to represent specific mountain wave events which enables future studies of the chemistry impact of local events even with a global model. The gravity wave temperature perturbations lead to increased chlorine activation and a corresponding reduction of species that react heterogeneously on PSCs as well as a zonal mean reduction of the ozone volume mixing ratio between 3% and 8% in the lower stratosphere, which is comparable to the results by Pierce et al. (2002).

The method as described in this study applies to OGWs only. An extension to non-orographic gravity waves would be desirable for the future, in order to be able to investigate the influence of weather systems like tropical storms, jets, fronts and convection on the chemistry (e.g., Wright, 2019; Zou et al., 2021).

For a comparison of the model with measurements, observations with appropriately high spatial resolution would be needed. Satellite measurements are typically averaged either in the vertical or in the horizontal and may have to be averaged in time to reduce the signal-to-noise ratio which could make it difficult to see the chemistry changes shown in this study using some instruments. Measurement campaigns like SOUTHTRAC-GW (Rapp et al., 2021) could help to assess and reduce errors in the model and compare the stochastic with the sub-stepping approach for specific case studies. While the sub-stepping of the chemistry decreases the overall performance of the model, it could be useful for detailed comparisons with airborne measurements where data at single time steps and grid points are needed. The stochastic approach leads to similar results on long-term averages but should not be used for comparisons at single grid points. Therefore, the latter could be useful for long-term simulations as it accounts for warm and cold phase of the gravity wave without impacting the model's computation time.

Consistent with previous studies like McDonald et al. (2009), the results of this study suggest that gravity-wave-induced temperature perturbations increase the period with chlorine activation, since we found the largest changes at the start and the end of the local winter. This work raises further questions that could be tackled by future simulations:

1. What is the impact of gravity wave temperature perturbations on ozone recovery?
2. Will there be an impact on dynamics like the shift of the polar vortex in the free-running simulations by Orr et al. (2020)?
3. What are the impacts at altitudes higher than 1 hPa?

Our study focused on stratospheric chemistry, but there are also changes in the troposphere. Further work is needed to investigate the tropospheric changes as they appear to be associated with dynamical rather than chemical changes. The $\hat{T}$ values in the mesosphere are expected to be even larger. With a different model set-up, the changes at these altitudes in the model could also be investigated and compared to previous studies investigating the interaction between gravity waves and the chemistry, especially in the mesosphere (e.g., Xu et al., 2000, 2003).

10.1029/2022MS003505

With simulations covering several decades, the impact of this new parameterization on ultra-violet radiation and the climate could be further investigated.

The response of WACCM's chemistry to the applied temperature perturbations is consistent with expectations from previous studies which were not able to account for this process interactively on a global scale. The method should be easy to implement in other chemistry-climate models as well. We hope that this study assists other chemistry climate researchers who seek to account for large-scale chemical impacts of subgrid-scale gravity wave temperature perturbations.

Appendix A: Orographic Gravity Wave Amplitude Scheme

A1. Background

The conceptual model behind our approach is 2D flow over an isolated obstacle, for example, Figure A1. We apply momentum flux conservation and wave saturation to this model following the approach of Lindzen (1981) for a single plane wave. The arguments below are familiar for the case of monochromatic waves (e.g., McFarlane, 1987). Here we simply attempt to highlight steps where the isolated obstacle geometry requires additional assumptions.

For steady-state 2D hydrostatic OGWs in uniform wind and stratification the vertical streamline displacement is given by:

$$\delta'(x,z) = h_s(x)\cos(Nz/U) + \mathrm{H}[h_s(x)]\sin(Nz/U), \tag{A1}$$

where U is the horizontal wind, N is the Brunt-Vaisalla frequency, $h_s(x)$ defines the obstacle surface elevation, and $\mathrm{H}[h_s(x)]$ is the Hilbert transform of $h_s(x)$ (Drazin & Su, 1975). Note for example, that for $h_s(x) = h_0\cos(kx)$ the Hilbert transform is $-h_0\sin(kx)$ and Equation A1 becomes the familiar monochromatic solution $\mathrm{Re}[h_0e^{i(kx+mz)}]$, where k and m are orographic horizontal and vertical wavenumbers, respectively.

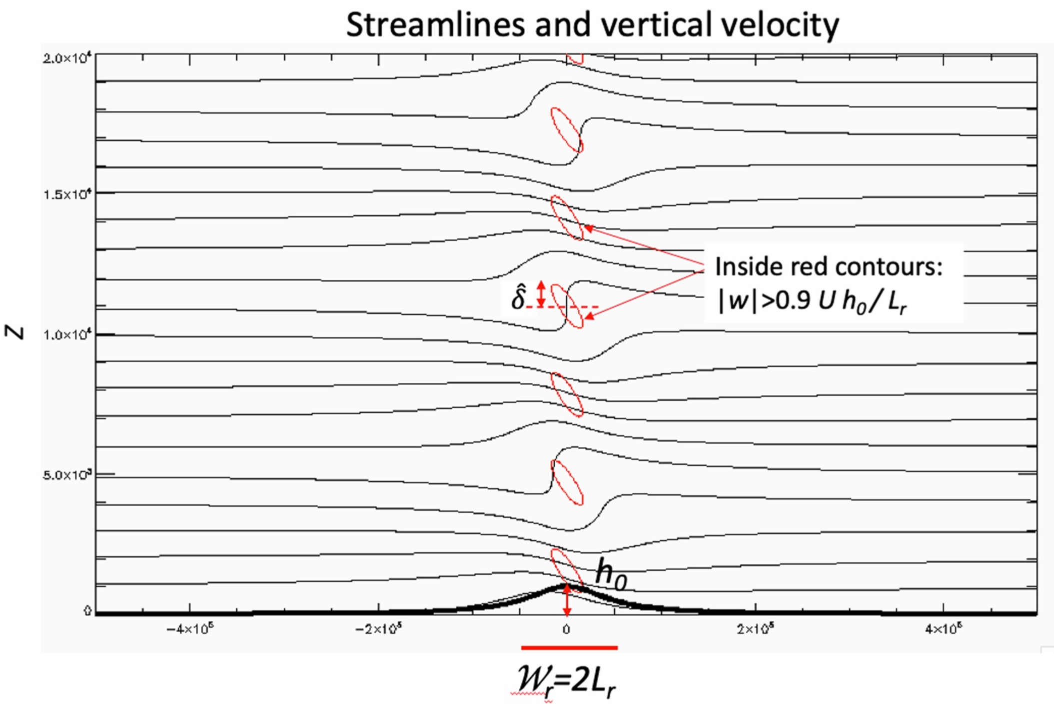

Figure A1. Linear, steady, hydrostatic 2D flow over a Witch-of-Agnesi obstacle $h_s(x) = h_0\,L_r^2/\left(L_r^2 + x^2\right)$. Uniform profiles of upstream horizontal wind U and stratification N are assumed. The solution shown uses an obstacle height $h_0 = U/N$. This is the saturated displacement amplitude (see text) so streamlines become vertical over the obstacle. Red ovals indicate where vertical velocity amplitude exceeds 0.9 Uh_0/L_r.

The streamline displacement can be used to derive expressions for perturbation horizontal and vertical winds

$$u' = -U \frac{\partial}{\partial_z} \delta' = \mathrm{Re}\left[-iN\delta'\right] \tag{A2}$$

$$w' = U \frac{\partial}{\partial_x} \delta' \propto U \frac{\hat{\delta}}{L_r} \propto 2U \frac{\hat{\delta}}{\mathcal{W}_r}, \tag{A3}$$

where L_r is the horizontal scale of the obstacle, $\mathcal{W}_r = 2L_r$ as in Figure A1, $\hat{\delta}$ is the peak displacement, and δ' is the displacement perturbation, see Appendix A3.

The expression in Equation A2 is exact and independent of the obstacle shape. In Equation A3 for general obstacle shapes, we must resort to plausible scaling arguments due to the form of Equation A1. In the special case of sinusoidal h_s we would obtain the exact relationship $w' = \mathrm{Re}[ikU\delta']$. Figure A1 shows that Equation A3 captures the relationship between $\hat{\delta}$ and peak values of w'.

The total stress produced by an isolated obstacle is given by

$$[\tau] = \int_{+\infty}^{-\infty} \rho u' w' \mathrm{d}x. \tag{A4}$$

This holds for any obstacle in any 2D flow. For hydrostatic flow, the wave perturbations are roughly confined to the region directly over the obstacle as is seen in Figure A1. $[\tau]$ is constant with height in the absence of wave dissipation, reflection or turning, a fact that is exploited in the derivation of wave drag schemes (Lindzen, 1981) and of the wave displacement algorithm (WDA) in Appendix A3.

We now scale and rewrite the integral at a particular level z in terms of the peak displacement $\hat{\delta}$,

$$\tau^*(z) = C\,\rho(z)\,U(z)\,N(z)\,\hat{\delta}(z)^2/\mathcal{W}_r \tag{A5}$$

where we have used Equation A3 and $u' \propto N\hat{\delta}$. C is a shape factor determined by the condition

$$\tau^* \times \mathcal{W}_r = [\tau] \tag{A6}$$

Equation A5 is the basis for the WDA described in Appendix A3.

We note that for the WDA there is no need to introduce $\mathcal{W}_r$ or C in Equation A5. We do so here to clarify the correspondence between the present approach and the earlier monochromatic wave approach in McFarlane (1987). Comparing Equation A5 with Equation 2.16 of McFarlane (1987) we see that the factor $C/\mathcal{W}_r$ in Equation A5 corresponds to the factor $k/2$ in the monochromatic formulation of McFarlane.

Further, for a Witch-of-Agnesi obstacle, Drazin and Su (1975) show that $C = \pi/4$. No single value of C is valid for general obstacles, but we expect C to be $O(1)$ for single peaked obstacles. In any event, the WDA requires only that C and $\mathcal{W}_r$ do not vary with z.

A2. Parameters Describing Unresolved Orography

The WDA in Appendix A3 needs parameters describing unresolved orography. Most critically, the WDA needs estimates of dominant ridge orientation θ_r and a ridge height h_r in each model grid point. The orientation θ_r is used to define the wavefront-perpendicular horizontal wind profile U. The height h_r is used as bottom forcing for the WDA.

These parameters are determined by a RFA (Appendix B). Figure B1 in particular shows that the RFA does a reasonable job of supplying θ_r and h_r. The RFA also calculates estimates of other quantities such as obstacle width $\mathcal{W}_r$, which can be used to derive OGW vertical velocity, but is not critical in the calculation of wave vertical displacement.

A3. Wave Displacement Algorithm

We adapt the approach of Lindzen (1981) to numerically derive profiles of τ^* and $\hat{\delta}$. The assumptions in Lindzen (1981) are well known and continue to form the basis for perhaps the majority of gravity wave drag schemes used in existing climate models. We summarize the key assumptions here for completeness: (a) The Wentzel–Kramers–Brillouin (WKB) approximation is valid; (b) Due to the parameterization working in a column, no wave reflection or turning occurs so the momentum flux τ is constant with height in the absence of dissipation; and (c) When wave overturning occurs precisely enough turbulent dissipation is produced to prevent further growth of wave amplitude with height. This is the "saturation hypothesis." Saturation is typically assumed to occur when $\hat{\delta} \propto U/N$. Note that here and throughout we are assuming the wave phase speed $c = 0$.

We now describe how the algorithm proceeds between two adjacent model interfaces in the vertical, l and $l+1$, with l increasing from the top of the model atmosphere to the surface. At level $l+1$ the OGW momentum flux is:

$$\tau^*_{l+1} = C \ \ \rho_{l+1} U_{l+1} N_{l+1} \hat{\delta}^2_{l+1} / \mathcal{W}_r \tag{A7}$$

where ρ_{l+1} is the atmospheric density, U_{l+1} is the horizontal wind normal to the wavefront, N_{l+1} is the Brunt-Vaisalla frequency, $\hat{\delta}_{l+1}$ is the peak wave-induced vertical streamline displacement, and $\mathcal{W}_r$ is as shown in Figure A1. At the level interface l immediately below $l+1$, a provisional momentum flux value is calculated assuming constant momentum flux in the absence of dissipation,

$$\tau^{*\dagger}_l = \tau^*_{l+1} - \mathcal{D}_l. \tag{A8}$$

Here $\mathcal{D}_l$ represents optional, weak dissipation of the momentum flux by processes such as radiative cooling or background diffusion. The latter is unimportant below the turbopause. The provisional momentum flux is inverted to give a provisional wave displacement at level interface l

$$\hat{\delta}^\dagger_l = \sqrt{\frac{\tau^{*\dagger}_l}{C \rho_l U_l N_l / \mathcal{W}_r}} \tag{A9}$$

The provisional displacement is then constrained by the saturation amplitude to give the final predicted displacement at l

$$\hat{\delta}_l = \mathrm{MIN}\left[\hat{\delta}^\dagger_l, U_l/N_l\right] \tag{A10}$$

which is then used to calculate the momentum flux at l

$$\tau^*_l = C \rho_l U_l N_l \hat{\delta}^2_l / \mathcal{W}_r. \tag{A11}$$

These calculations (Equations A7–A11) are performed beginning in a source super-layer (described below) to the top of the model. The algorithm is closed by setting the wave displacement in the source super-layer,

$$\hat{\delta}_{\mathrm{src}} = \mathrm{MIN}\left(h_r, F_c \frac{U_{\mathrm{src}}}{N_{\mathrm{src}}}\right), \tag{A12}$$

where h_r is an estimated obstacle height for the unresolved orography determined by the RFA (Appendix B). F_c is a critical inverse Froude number which we set equal to 1. The estimate h_r is meant to correspond to h_0 in Figure A1, although the RFA makes no assumption about obstacle shape.

It is worth reiterating that in the absence of dissipation (Equation A8) the resulting profile of $\hat{\delta}_l$ given by Equations A7–A12 is completely independent of $\mathcal{W}_r$ or C, as long as these quantities are independent of height.

A3.1. Flow Blocking Layer

The flow blocking layer is a super-layer comprised of layers with

$$\hat{Z}_l \le h_r \tag{A13}$$

where $\hat{Z}_l$ is the height of lth interface (this is the upper interface for layer l). Within the blocking layer, pressure weighted averages of winds and stratification are calculated. These are used to define the orographic inverse Froude number,

$$F = \frac{N_{\mathrm{src}} h_r}{U_{\mathrm{src}}}. \tag{A14}$$

F is then used to identify low-level regimes as done in Scinocca and McFarlane (2000) except that we use $F_c = 1$ rather than 0.7.

This algorithm is simple and can provide only an approximation of stratospheric wave amplitudes. In addition to inaccuracy related to the specification of amplitude and orientation in the forcing data, there are also errors related to the simplified picture of wave propagation assumed. Importantly, the present scheme in Equations A7–A12 assumes purely vertical propagation of wave activity within a single model column. It is well known that this is not the case and even for grid boxes of $\sim(100\ \mathrm{km})^2$ we should expect significant horizontal transfer of wave activity into neighboring model columns (Eckermann et al., 2015).

Appendix B: Orographic Forcing for WACCM/CESM

As described in Lauritzen et al. (2015) generation of orographic forcing for CESM involves two major steps. First, a high-resolution global digital elevation model on a lat-lon grid (typically 30 arc-second resolution) is binned onto an approximately uniform 3,000 × 3,000 × 6 intermediate cubed-sphere grid which Lauritzen et al. refer to as the A-grid. The A-grid is on gnomonic coordinates and has an approximately uniform spatial resolution of 3 km.

Next, the global orography on the A-grid, which we denote by $h(A)$, is smoothed horizontally by some amount to produce a smoothed orography $\overline{h}(A)$. Orography smoothing is a poorly documented aspect of atmospheric modeling (Elvidge et al., 2019). In the case of CESM, dynamical core developers recommend smoothing amounts, which are reproduced using rigorously defined smoothing operators working on A-grid gnomonic coordinates. In the case of the lat-lon finite-volume dynamical with 0.9°latitude × 1.25°longitude resolution the amount of smoothing applied is equivalent to convolution using a circular conical kernel with a radius R_{sm} of around 180 km. The A-grid orography $h(A)$ and the smoothed orography $\overline{h}(A)$ are shown in Figures B1a and B1b. The smoothed orography $\overline{h}(A)$ is conservatively regridded to the model computational grid to form the grid-mean lower boundary geopotential $\Phi = g\ \overline{h}$ for the model.

B1. Unresolved Orography and Ridge-Finding Algorithm (RFA)

Forcing for the OGW parameterizations used in CESM/WACCM are derived from the unresolved orography

$$h'(A) = h(A) - \overline{h}(A) \tag{B1}$$

which is shown in Figure B1c.

A RFA is applied to the unresolved orography $h'(A)$. The RFA is a heuristic procedure intended to capture the orientation, height and size of orographic ridges that a human observer would identify, and is likely sub-optimal in many respects. However, the final product of the RFA (Figure B1d) does succeed in capturing the salient features of the Southern Andes. Most importantly for the present study the RFA captures ridge height and orientation. The RFA used here is related in general approach to that described by Bacmeister et al. (1994) and Eckermann et al. (2004), but differs in detail. In addition, the RFA produces gridded output for use in an atmospheric model instead of grid independent forcings like those in the studies cited.

The RFA is a two stage process. In the first stage, a thinned list of local maxima in $h'(A)$ is created. At each of these locations (a_{0i}, b_{0i}) directional variance is analyzed at 16 equally spaced angles θ_r between 0 and 168.75° in gnomonic coordinates. Square sections are used with sides of approximately $R_{\mathrm{sm}}/\sqrt{2}$. The optimal orientation is that for which the ridge profile variance explains the largest fraction of the total variance in the section. Next the b'-averaged "ridge profile" and a'-averaged "crest profile" are used to find a location (a_{1i}, b_{1i}) closer to the crest of the diagnosed ridge. At this new location the RFA re-calculates new ridge quantities.

10.1029/2022MS003505

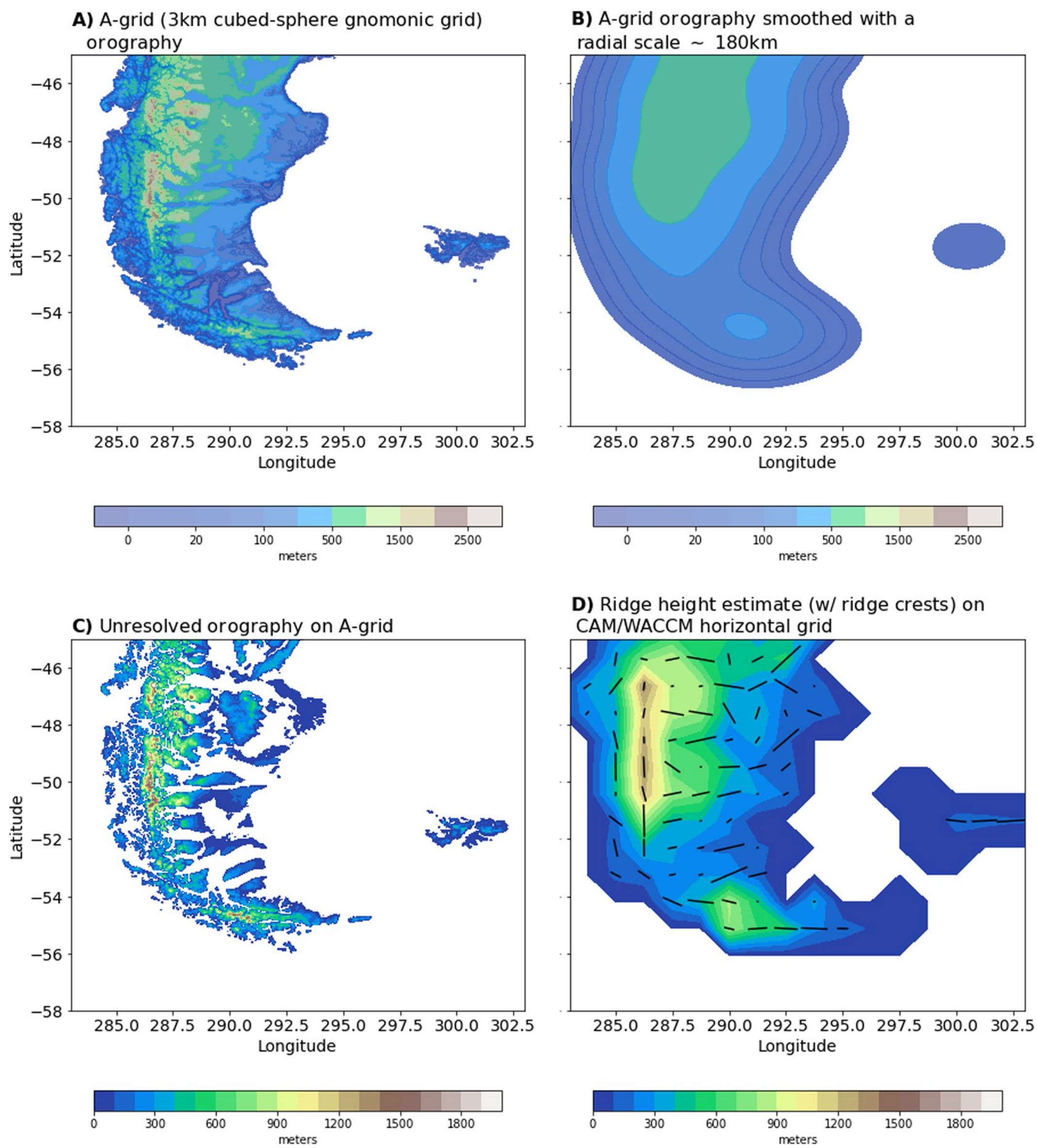

Figure B1. Stages in processing of orographic forcing files for Community Earth System Model illustrated over the Southern Andes. (a) Unsmoothed orography on A-grid $h(A)$ (see text); (b) Smoothed orography $\overline{h}(A)$. Amount of smoothing applied is equivalent to convolution with circular conical kernel with a smoothing radius $R_{\mathrm{sm}} \approx 180$ km. This smoothed orography is conservatively regridded to give the lower boundary elevation for 0.9° × 1.25° Whole Atmosphere Community Climate Model (WACCM). (c) Unresolved orography $h'(A)$ on A-grid. (d) End-result of Ridge Finding Algorithm (RFA). Color shading shows mean ridge height estimate from the RFA on 0.9° × 1.25° grid. Black lines show length and orientation of diagnosed ridge crests.

An example of the first stage is shown in Figure B2 in the Southern Andes.

Here the RFA identifies a dominant orientation $\theta_r = 112.5°$ clockwise from the b-axis in gnomonic coordinates. The associated ridge elevation profile, $\overline{h'(a')}^{b'}$, is shown in Figure B2b. The RFA calculates an obstacle height using:

$$h_r = \mathrm{MAX}\left[\overline{h'(a')}^{b'}\right] - \mathrm{MIN}\left[\overline{(h'(a')}^{b'}\right],$$

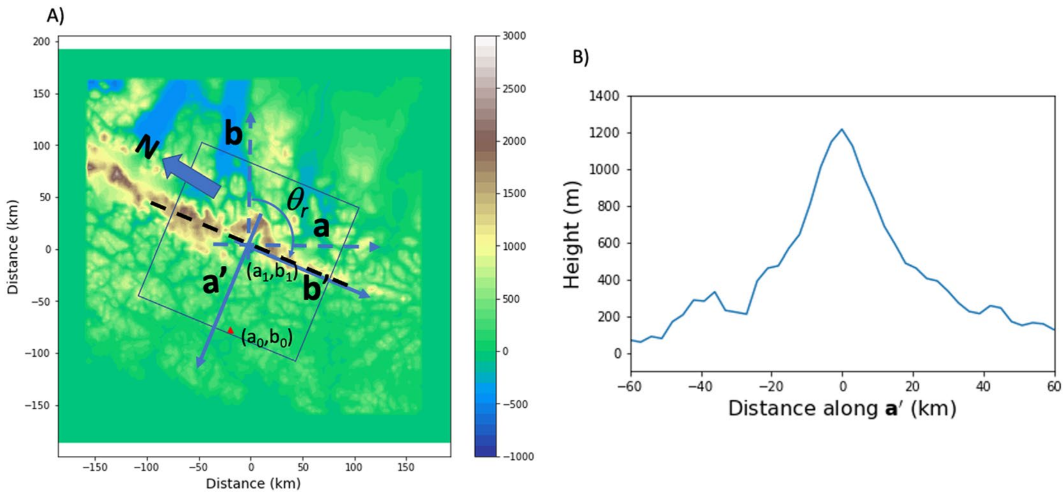

Figure B2. Sample ridge analysis. (a) Section of unresolved orography $h'(A)$ in the Southern Andes centered near 73.4°W, 50.4°S. The plot is shown in scaled gnomonic coordinates (a, b) on the southern face of a cubed sphere. The direction of true north near the center of the domain is indicated by the thick arrow. The (a', b') axes indicate a clockwise rotation of 112.5°. The box shows the domain used in the variance analysis. (b) Ridge elevation profile. Blue line shows b'-averaged elevation profile as a function of a' for the box in (a).

which for the feature shown in Figure B2b is ≈1,140 m. Visual inspection of h_r and θ_r returned by the RFA compared with maps of $h'(A)$ suggests that these quantities are well captured globally.

The first stage of the RFA results in an accumulation of (a_{1i}, b_{1i}) points along ridge crests in the A-grid. In addition to an orientation θ_r and estimated obstacle height h_r, each point is also associated with an obstacle width $\mathcal{W}_r$, along-ridge length l_r, and ridge "quality" $\mathcal{Q}_r$, the fractional variance explained by the ridge. There is significant redundancy in the sense that multiple (a_{1i}, b_{1i}) points may cluster over the same feature.

In the second stage of the RFA the features at (a_{1i}, b_{1i}) points are thinned spatially using a function of h_r, l_r, and $\mathcal{Q}_r$ to select the "best" feature in regions with dimensions $\sim R_{\mathrm{sm}}/\sqrt{2}$. The surviving features are then aggregated into 16 directional bins within each model grid box according to the θ_r of each feature. In this analysis only the bin with the highest value of $A_r = h_r\, l_r$ is used. These are the features plotted in Figure B1d.

Appendix C: Data Sets

As discussed in Section 3, we compare the WACCM $\hat{T}$ with COSMIC satellite measurements and ERA5 reanalysis data which are briefly summarized in this section, together with the method to derive the gravity wave temperature perturbations from the temperature fields of each data set.

C1. COSMIC

COSMIC (Rocken et al., 2000) provided high-precision global positioning system-based radio occultation measurements of temperature and humidity with an uncertainty of less than 1 K (Scherllin-Pirscher et al., 2011). Since the measuring satellite in low-Earth orbit could receive signals from whichever Global Positioning System (GPS) satellite is in its view, the profiles are scattered irregularly in time and location on Earth. COSMIC provided nearly global coverage each day with higher density in the mid-latitudes (L. Wang & Alexander, 2010). Additionally, the vertical resolution of about 1 km for wave observations makes the measurements suitable for investigation of gravity waves in the atmosphere (e.g., Scherllin-Pirscher et al., 2021; Schmidt et al., 2016). The measurements are reliable in the stratosphere up to 38 km altitude (L. Wang & Alexander, 2010) and the mission covered the period from mid 2006 to mid 2020. Horizontal resolution is limited to about 100 km due to LOS integration in the limb-like viewing geometry which makes GPS radio occultation measurements sensitive to horizontal wavelengths larger than about 200 km (e.g., Kursinski et al., 1997). Depending on the orientation of the gravity wave to the

LOS, shorter scale gravity wave amplitudes are underestimated by radio occultation measurements, as described for example, by Schmidt et al. (2016).

In order to derive gravity wave properties from the COSMIC temperature measurements, it is necessary to separate planetary waves, such as Kelvin and Rossby waves, from the gravity waves of interest here. We apply the method by L. Wang and Alexander (2010) to the COSMIC measurements which consists of a binning of the data to a 15×10 longitude-latitude grid for each level ($\approx 1{,}600 \times 1{,}100$ km^2 at the equator), applying a longitude-dependent Stockwell-transform (Stockwell et al., 1996) to each altitude and latitude bin, interpolating the temperatures back to the profile locations and subtracting this large-scale signal from the original measurements. The coverage of the measurements requires the large-scale temperature to be defined by zonal wavenumbers 0–6 (L. Wang & Alexander, 2010). Thus, this removes the largest wavelengths from the temperature, but remnants of planetary waves might still remain in the resulting temperature perturbations. As suggested by L. Wang and Alexander (2010), we bin the temperatures on a daily basis, but we use a sine fit or (where both are impossible) a nearest neighbor interpolation with four neighbors to fill remaining gaps. We use the "wet" temperature profiles which account for humidity and can therefore be used at lower altitudes than the dry retrievals.

C2. ERA5

Since publication of the fifth generation reanalysis product by ECMWF ERA5 (Hersbach et al., 2020), it has been shown that it is able to directly resolve a large fraction of gravity waves (Dörnbrack, 2021; Dörnbrack et al., 2022; Kaifler et al., 2020) although it will be missing or underestimating amplitudes of short horizontal wavelength OGW (Hoffmann et al., 2017; Kruse et al., 2022). Therefore, it is suitable as a reference for gravity wave studies. In contrast to satellite measurements, it provides hourly global coverage.

In the method by Dörnbrack et al. (2022), gravity wave temperature perturbations are extracted from the ERA5 data by removing a large-scale field by filtering via triangular truncation at total wavenumber 21 (T 21) from the full spectral resolution output of ERA5. This ensures that the temperature perturbations consist of horizontal wavenumbers larger than 22, that is, wavelengths smaller than about 1,000 km at 60°S/N (Gupta et al., 2021). The horizontal grid spacing of 0.28125° ($\approx$25 km) and an effective resolution of 6 times the grid length means that only wavelengths larger than about 150 km are reliably represented.

Gravity waves in ERA5 have been shown to be resolved up to 1 hPa although gravity waves are damped in the model starting at lower altitudes to avoid unphysical effects at the model top (Ehard et al., 2018). In addition, clear wave signatures can be expected in the stratosphere only because tropospheric signatures are dominated by mesoscale modes such as flow over mountains or weather systems. In order to minimize both effects, we limit our analysis to pressure levels between 5 and 100 hPa, which corresponds roughly to the altitude range from 14 to 34 km.

Data Availability Statement

COSMIC data are downloaded from UCAR COSMIC Program (2006). ERA5 data are downloaded using the Climate Data Store (CDS) API (Hersbach et al., 2017). Model simulation data and the scripts used to create the figures are available online (Weimer et al., 2023) using the following link: https://www.acom.ucar.edu/DOI-DATA/dkin/JAMES_Weimer_2022. The model code (software) modifications to add the parameterization to the published version of CESM2.1.1 (see Danabasoglu et al., 2020) can also be found using this link.

Acknowledgments

This work is supported by grant AGS-1906719 from the Atmospheric Chemistry Division of the U.S. National Science Foundation (NSF). MJA is supported by NASA Grant 80NSSC20K0950. This material is based upon work supported by National Center for Atmospheric Research (NCAR), which is a major facility sponsored by NSF under the Cooperative Agreement 1852977. Parts of this study are generated using Copernicus Climate Change Service information [2022]. Neither the European Commission nor ECMWF is responsible for any use that may be made of the Copernicus information or data it contains. The CESM project is supported primarily by NSF. We would like to acknowledge high-performance computing and data storage support from Cheyenne and Casper provided by NCAR's Computational and Information Systems Laboratory (2019), sponsored by NSF.

References

Alexander, M. J. (2015). Global and seasonal variations in three-dimensional gravity wave momentum flux from satellite limb-sounding temperatures. *Geophysical Research Letters*, *42*(16), 6860–6867. https://doi.org/10.1002/2015GL065234

Alexander, S. P., Klekociuk, A. R., & Tsuda, T. (2009). Gravity wave and orographic wave activity observed around the Antarctic and Arctic stratospheric vortices by the COSMIC GPS-RO satellite constellation. *Journal of Geophysical Research*, *114*(D17), D17103. https://doi.org/10.1029/2009JD011851

Anthes, R. A., Bernhardt, P. A., Chen, Y., Cucurull, L., Dymond, K. F., Ector, D., et al. (2008). The COSMIC/FORMOSAT-3 Mission: Early results. *Bulletin of the American Meteorological Society*, *89*(3), 313–334. https://doi.org/10.1175/BAMS-89-3-313

Bacmeister, J. T., Eckermann, S. D., Tsias, A., Carslaw, K. S., & Peter, T. (1999). Mesoscale temperature fluctuations induced by a spectrum of gravity waves: A comparison of parameterizations and their impact on stratospheric microphysics. *Journal of the Atmospheric Sciences*, *56*(12), 1913–1924. https://doi.org/10.1175/1520-0469(1999)056<1913:MTFIBA>2.0.CO;2

Bacmeister, J. T., Newman, P. A., Gary, B. L., & Chan, K. R. (1994). An algorithm for forecasting mountain wave-related turbulence in the stratosphere. *Weather and Forecasting*, *9*(2), 241–253. https://doi.org/10.1175/1520-0434(1994)009<0241:AAFFMW>2.0.CO;2

Barahona, D., Molod, A., Bacmeister, J., Nenes, A., Gettelman, A., Morrison, H., et al. (2014). Development of two-moment cloud microphysics for liquid and ice within the NASA Goddard Earth Observing System Model (GEOS-5). *Geoscientific Model Development*, *7*(4), 1733–1766. https://doi.org/10.5194/gmd-7-1733-2014

Burkholder, J. B., Sander, S. P., Abbatt, J. P. D., Barker, J. R., Huie, R. E., Kolb, C. E., et al. (2015). *Chemical kinetics and photochemical data for use in atmospheric studies: Evaluation Number 18* (Tech. Rep.). Jet Propulsion Laboratory.

Carslaw, K. S., Luo, B. P., Clegg, S. L., Peter, T., Brimblecombe, P., & Crutzen, P. J. (1994). Stratospheric aerosol growth and HNO_3 gas phase depletion from coupled HNO_3 and water uptake by liquid particles. *Geophysical Research Letters*, *21*(23), 2479–2482. https://doi.org/10.1029/94GL02799

Carslaw, K. S., Wirth, M., Tsias, A., Luo, B. P., Dörnbrack, A., Leutbecher, M., et al. (1998). Increased stratospheric ozone depletion due to mountain-induced atmospheric waves. *Nature*, *391*(6668), 675–678. https://doi.org/10.1038/35589

Computational and Information Systems Laboratory. (2019). *Cheyenne: HPE/SGI ICE XA System (University Community Computing)* (Tech. Rep.). National Center for Atmospheric Research. https://doi.org/10.5065/D6RX99HX

Considine, D. B., Douglass, A. R., Connell, P. S., Kinnison, D. E., & Rotman, D. A. (2000). A polar stratospheric cloud parameterization for the global modeling initiative three-dimensional model and its response to stratospheric aircraft. *Journal of Geophysical Research*, *105*(D3), 3955–3973. https://doi.org/10.1029/1999JD900932

Danabasoglu, G., Lamarque, J. F., Bacmeister, J., Bailey, D. A., DuVivier, A. K., Edwards, J., et al. (2020). The Community Earth System Model Version 2 (CESM2). *Journal of Advances in Modeling Earth Systems*, *12*(2), e2019MS001916. https://doi.org/10.1029/2019MS001916

Das, U., & Pan, C. J. (2013). Strong Kelvin wave activity observed during the westerly phase of QBO - A case study. *Annales Geophysicae*, *31*(4), 581–590. https://doi.org/10.5194/ANGEO-31-581-2013

Dean, S. M., Flowerdew, J., Lawrence, B. N., & Eckermann, S. D. (2007). Parameterisation of orographic cloud dynamics in a GCM. *Climate Dynamics*, *28*(6), 581–597. https://doi.org/10.1007/s00382-006-0202-0

Dörnbrack, A. (2021). Stratospheric mountain waves trailing across Northern Europe. *Journal of the Atmospheric Sciences*, *78*(9), 2835–2857. https://doi.org/10.1175/JAS-D-20-0312.1

Dörnbrack, A., Eckermann, S. D., Williams, B. P., & Haggerty, J. (2022). Stratospheric gravity waves excited by a propagating Rossby wave train—A DEEPWAVE case study. *Journal of the Atmospheric Sciences*, *79*(2), 567–591. https://doi.org/10.1175/JAS-D-21-0057.1

Dörnbrack, A., Gisinger, S., Pitts, M. C., Poole, L. R., & Maturilli, M. (2017). Multilevel cloud structures over Svalbard. *Monthly Weather Review*, *145*(4), 1149–1159. https://doi.org/10.1175/MWR-D-16-0214.1

Dörnbrack, A., Kaifler, B., Kaifler, N., Rapp, M., Wildmann, N., Garhammer, M., et al. (2020). Unusual appearance of mother-of-pearl clouds above El Calafate, Argentina (50°21′S, 72°16′W). *Weather*, *75*(12), 378–388. https://doi.org/10.1002/wea.3863

Drazin, P. G., & Su, C. H. (1975). A note on long-wave theory of airflow over a mountain. *Journal of the Atmospheric Sciences*, *32*(2), 437–439. https://doi.org/10.1175/1520-0469(1975)032<0437:ANOLWT>2.0.CO;2

Eckermann, S. D., Broutman, D., & Ma, J. (2004). *The NRL Mountain Wave Forecast Model (MWFM)* (Technical Report No. NRL/MR/7540-04-8733). Naval Research Laboratory.

Eckermann, S. D., Dörnbrack, A., Flentje, H., Vosper, S. B., Mahoney, M. J., Bui, T. P., & Carslaw, K. S. (2006). Mountain wave-induced polar stratospheric cloud forecasts for aircraft science flights during SOLVE/THESEO 2000. *Weather and Forecasting*, *21*(1), 42–68. https://doi.org/10.1175/WAF901.1

Eckermann, S. D., Ma, J., & Broutman, D. (2015). Effects of horizontal geometrical spreading on the parameterization of orographic gravity wave drag. Part I: Numerical transform solutions. *Journal of the Atmospheric Sciences*, *72*(5), 2330–2347. https://doi.org/10.1175/JAS-D-14-0129.1

Ehard, B., Malardel, S., Dörnbrack, A., Kaifler, B., Kaifler, N., & Wedi, N. (2018). Comparing ECMWF high-resolution analyses with lidar temperature measurements in the middle atmosphere. *Quarterly Journal of the Royal Meteorological Society*, *144*(712), 633–640. https://doi.org/10.1002/qj.3206

Elvidge, A. D., Sandu, I., Wedi, N., Vosper, S. B., Zadra, A., Boussetta, S., et al. (2019). Uncertainty in the representation of orography in weather and climate models and implications for parameterized drag. *Journal of Advances in Modeling Earth Systems*, *11*(8), 2567–2585. https://doi.org/10.1029/2019ms001661

Emmons, L. K., Schwantes, R. H., Orlando, J. J., Tyndall, G., Kinnison, D., Lamarque, J.-F., et al. (2020). The Chemistry Mechanism in the Community Earth System Model Version 2 (CESM2). *Journal of Advances in Modeling Earth Systems*, *12*(4), e2019MS001882. https://doi.org/10.1029/2019MS001882

Eyring, V., Bony, S., Meehl, G. A., Senior, C. A., Stevens, B., Stouffer, R. J., & Taylor, K. E. (2016). Overview of the Coupled Model Intercomparison Project Phase 6 (CMIP6) experimental design and organization. *Geoscientific Model Development*, *9*(5), 1937–1958. https://doi.org/10.5194/GMD-9-1937-2016

Fritts, D. C., & Alexander, M. J. (2003). Gravity wave dynamics and effects in the middle atmosphere. *Reviews of Geophysics*, *41*(1), 1003. https://doi.org/10.1029/2001RG000106

Fueglistaler, S., Buss, S., Luo, B. P., Wernli, H., Flentje, H., Hostetler, C. A., et al. (2003). Detailed modeling of mountain wave PSCs. *Atmospheric Chemistry and Physics*, *3*(3), 697–712. https://doi.org/10.5194/acp-3-697-2003

Garcia, R. R., Smith, A. K., Kinnison, D. E., de la Cámara, A., & Murphy, D. J. (2017). Modification of the gravity wave parameterization in the Whole Atmosphere Community Climate Model: Motivation and results. *Journal of the Atmospheric Sciences*, *74*(1), 275–291. https://doi.org/10.1175/JAS-D-16-0104.1

Gelaro, R., McCarty, W., Suárez, M. J., Todling, R., Molod, A., Takacs, L., et al. (2017). The Modern-Era Retrospective Analysis for Research and Applications, Version 2 (MERRA-2). *Journal of Climate*, *30*(14), 5419–5454. https://doi.org/10.1175/JCLI-D-16-0758.1

Gettelman, A., Mills, M. J., Kinnison, D. E., Garcia, R. R., Smith, A. K., Marsh, D. R., et al. (2019). The Whole Atmosphere Community Climate Model Version 6 (WACCM6). *Journal of Geophysical Research: Atmospheres*, *124*(23), 12380–12403. https://doi.org/10.1029/2019JD030943

Giorgetta, M. A., Brokopf, R., Crueger, T., Esch, M., Fiedler, S., Helmert, J., et al. (2018). ICON-A, the atmosphere component of the ICON Earth System Model: I. Model description. *Journal of Advances in Modeling Earth Systems*, *10*(7), 1613–1637. https://doi.org/10.1029/2017MS001242

Gupta, A., Birner, T., Dörnbrack, A., & Polichtchouk, I. (2021). Importance of gravity wave forcing for springtime southern polar vortex breakdown as revealed by ERA5. *Geophysical Research Letters*, *48*(10), e2021GL092762. https://doi.org/10.1029/2021GL092762

Hanson, D., & Mauersberger, K. (1988). Laboratory studies of the nitric acid trihydrate: Implications for the south polar stratosphere. *Geophysical Research Letters*, *15*(8), 855–858. https://doi.org/10.1029/GL015I008P00855

Hendricks, E. A., Doyle, J. D., Eckermann, S. D., Jiang, Q., & Reinecke, P. A. (2014). What is the source of the stratospheric gravity wave belt in austral winter? *Journal of the Atmospheric Sciences*, *71*(5), 1583–1592. https://doi.org/10.1175/JAS-D-13-0332.1

Hersbach, H., Bell, B., Berrisford, P., Hirahara, S., Horányi, A., Muñoz Sabater, J., et al. (2020). The ERA5 global reanalysis. *Quarterly Journal of the Royal Meteorological Society*, *146*(730), 1999–2049. https://doi.org/10.1002/qj.3803

Hersbach, H., Bell, B., Berrisford, P., Hirahara, S., Horányi, A., Muñoz-Sabater, J., et al. (2017). *Complete ERA5: Fifth generation of ECMWF atmospheric reanalyses of the global climate*. Copernicus Climate Change Service (C3S) Data Store (CDS).

Hertzog, A., Alexander, J. M., & Plougonven, R. (2012). On the intermittency of gravity wave momentum flux in the stratosphere. *Journal of the Atmospheric Sciences*, *69*(11), 3433–3448. https://doi.org/10.1175/JAS-D-12-09.1

Hindley, N. P., Wright, C. J., Gadian, A. M., Hoffmann, L., Hughes, J. K., Jackson, D. R., et al. (2021). Stratospheric gravity waves over the mountainous island of South Georgia: Testing a high-resolution dynamical model with 3-D satellite observations and radiosondes. *Atmospheric Chemistry and Physics*, *21*(10), 7695–7722. https://doi.org/10.5194/acp-21-7695-2021

Hoffmann, L., & Alexander, M. J. (2009). Retrieval of stratospheric temperatures from Atmospheric Infrared Sounder radiance measurements for gravity wave studies. *Journal of Geophysical Research*, *114*(D7), D07105. https://doi.org/10.1029/2008JD011241

Hoffmann, L., Günther, G., Li, D., Stein, O., Wu, X., Griessbach, S., et al. (2019). From ERA-interim to ERA5: The considerable impact of ECMWF's next-generation reanalysis on Lagrangian transport simulations. *Atmospheric Chemistry and Physics*, *19*(5), 3097–3124. https://doi.org/10.5194/acp-19-3097-2019

Hoffmann, L., Spang, R., Orr, A., Alexander, M. J., Holt, L. A., & Stein, O. (2017). A decadal satellite record of gravity wave activity in the lower stratosphere to study polar stratospheric cloud formation. *Atmospheric Chemistry and Physics*, *17*(4), 2901–2920. https://doi.org/10.5194/acp-17-2901-2017

Hoffmann, L., Xue, X., & Alexander, M. J. (2013). A global view of stratospheric gravity wave hotspots located with Atmospheric Infrared Sounder observations. *Journal of Geophysical Research: Atmospheres*, *118*(2), 416–434. https://doi.org/10.1029/2012JD018658

Höpfner, M., Larsen, N., Spang, R., Luo, B. P., Ma, J., Svendsen, S. H., et al. (2006). MIPAS detects Antarctic stratospheric belt of NAT PSCs caused by mountain waves. *Atmospheric Chemistry and Physics*, *6*(5), 1221–1230. https://doi.org/10.5194/acp-6-1221-2006

Jackson, D. R., Gadian, A., Hindley, N. P., Hoffmann, L., Hughes, J., King, J., et al. (2018). The South Georgia Wave Experiment: A means for improved analysis of gravity waves and low-level wind impacts generated from mountainous islands. *Bulletin of the American Meteorological Society*, *99*(5), 1027–1040. https://doi.org/10.1175/BAMS-D-16-0151.1

Joos, H., Spichtinger, P., Lohmann, U., Gayet, J.-F., & Minikin, A. (2008). Orographic cirrus in the global climate model ECHAM5. *Journal of Geophysical Research*, *113*(D18), D18205. https://doi.org/10.1029/2007JD009605

Kaifler, N., Kaifler, B., Dörnbrack, A., Rapp, M., Hormaechea, J. L., & de la Torre, A. (2020). Lidar observations of large-amplitude mountain waves in the stratosphere above Tierra del Fuego, Argentina. *Scientific Reports*, *10*(1), 1–10. https://doi.org/10.1038/s41598-020-71443-7

Kärcher, B., Jensen, E. J., & Lohmann, U. (2019). The impact of mesoscale gravity waves on homogeneous ice nucleation in cirrus clouds. *Geophysical Research Letters*, *46*(10), 5556–5565. https://doi.org/10.1029/2019GL082437

Kay, J. E., Deser, C., Phillips, A., Mai, A., Hannay, C., Strand, G., et al. (2015). The Community Earth System Model (CESM) large ensemble project: A community resource for studying climate change in the presence of internal climate variability. *Bulletin of the American Meteorological Society*, *96*(8), 1333–1349. https://doi.org/10.1175/BAMS-D-13-00255.1

Kinnison, D. E., Brasseur, G. P., Walters, S., Garcia, R. R., Marsh, D. R., Sassi, F., et al. (2007). Sensitivity of chemical tracers to meteorological parameters in the MOZART-3 chemical transport model. *Journal of Geophysical Research*, *112*(D20), 20302. https://doi.org/10.1029/2006JD007879

Knippertz, P., Gehne, M., Kiladis, G. N., Kikuchi, K., Satheesh, A. R., Roundy, P. E., et al. (2022). The intricacies of identifying equatorial waves. *Quarterly Journal of the Royal Meteorological Society*, *148*(747), 2814–2852. https://doi.org/10.1002/QJ.4338

Krisch, I., Preusse, P., Ungermann, J., Dörnbrack, A., Eckermann, S. D., Ern, M., et al. (2017). First tomographic observations of gravity waves by the infrared limb imager GLORIA. *Atmospheric Chemistry and Physics*, *17*(24), 14937–14953. https://doi.org/10.5194/ACP-17-14937-2017

Kruse, C. G., Alexander, M. J., Hoffmann, L., van Niekerk, A., Polichtchouk, I., Bacmeister, J. T., et al. (2022). Observed and modeled mountain waves from the surface to the mesosphere near the Drake Passage. *Journal of the Atmospheric Sciences*, *79*(4), 909–932. https://doi.org/10.1175/JAS-D-21-0252.1

Kursinski, E. R., Hajj, G. A., Schofield, J. T., Linfield, R. P., & Hardy, K. R. (1997). Observing Earth's atmosphere with radio occultation measurements using the Global Positioning System. *Journal of Geophysical Research*, *102*(D19), 23429–23465. https://doi.org/10.1029/97JD01569

Lauritzen, P. H., Bacmeister, J. T., Callaghan, P. F., & Taylor, M. A. (2015). NCAR global model topography generation software for unstructured grids. *Geoscientific Model Development Discussions*, *8*(6), 4623–4651.

Leena, P. P., Venkat Ratnam, M., Krishna Murthy, B. V., & Vijaya Bhaskara Rao, S. (2012). Detection of high frequency gravity waves using high resolution radiosonde observations. *Journal of Atmospheric and Solar-Terrestrial Physics*, *77*, 254–259. https://doi.org/10.1016/J.JASTP.2012.01.003

Lilly, D. K., Nicholls, J. M., Kennedy, P. J., Klemp, J. B., & Chervin, R. M. (1982). Aircraft measurements of wave momentum flux over the Colorado Rocky Mountains. *Quarterly Journal of the Royal Meteorological Society*, *108*(457), 625–642. https://doi.org/10.1002/QJ.49710845709

Lindzen, R. S. (1981). Turbulence and stress owing to gravity wave and tidal breakdown. *Journal of Geophysical Research*, *86*(C10), 9707–9714. https://doi.org/10.1029/JC086iC10p09707

Madden, R. A. (1979). Observations of large-scale traveling Rossby waves. *Reviews of Geophysics*, *17*(8), 1935–1949. https://doi.org/10.1029/RG017I008P01935

Mann, G. W., Carslaw, K. S., Chipperfield, M. P., Davies, S., & Eckermann, S. D. (2005). Large nitric acid trihydrate particles and denitrification caused by mountain waves in the Arctic stratosphere. *Journal of Geophysical Research*, *110*(D8), D08202. https://doi.org/10.1029/2004JD005271

Marti, J., & Mauersberger, K. (1993). A survey and new measurements of ice vapor pressure at temperatures between 170 and 250K. *Geophysical Research Letters*, *20*(5), 363–366. https://doi.org/10.1029/93GL00105

McDonald, A. J., George, S. E., & Woollands, R. M. (2009). Can gravity waves significantly impact PSC occurrence in the Antarctic? *Atmospheric Chemistry and Physics*, *9*(22), 8825–8840. https://doi.org/10.5194/acp-9-8825-2009

McFarlane, N. A. (1987). The effect of orographically excited gravity wave drag on the general circulation of the lower stratosphere and troposphere. *Journal of the Atmospheric Sciences*, *44*(14), 1775–1800. https://doi.org/10.1175/1520-0469(1987)044<1775:TEOOEG>2.0.CO;2

Murphy, D. M., & Ravishankara, A. R. (1994). Temperature averages and rates of stratospheric reactions. *Geophysical Research Letters*, *21*(23), 2471–2474. https://doi.org/10.1029/94GL02287

Noel, V., & Pitts, M. (2012). Gravity wave events from mesoscale simulations, compared to polar stratospheric clouds observed from spaceborne lidar over the Antarctic Peninsula. *Journal of Geophysical Research*, *117*(D11), D11207. https://doi.org/10.1029/2011JD017318

Orr, A., Hosking, J. S., Delon, A., Hoffmann, L., Spang, R., Moffat-Griffin, T., et al. (2020). Polar stratospheric clouds initiated by mountain waves in a global chemistry–climate model: A missing piece in fully modelling polar stratospheric ozone depletion. *Atmospheric Chemistry and Physics*, *20*(21), 12483–12497. https://doi.org/10.5194/acp-20-12483-2020

Pierce, R. B., Al-Saadi, J., Fairlie, T. D., Natarajan, M., Harvey, V. L., Grose, W. L., et al. (2002). Large-scale chemical evolution of the Arctic vortex during the 1999/2000 winter: HALOE/POAM III Lagrangian photochemical modeling for the SAGE III—Ozone Loss and Validation Experiment (SOLVE) campaign. *Journal of Geophysical Research*, *107*(D5), SOL60-1–SOL60-26. https://doi.org/10.1029/2001JD001063

Polichtchouk, I., van Niekerk, A., & Wedi, N. (2022). Resolved gravity waves in the extra-tropical stratosphere: Effect of horizontal resolution increase from O(10 km) to O(1 km). *Journal of the Atmospheric Sciences*, *80*(2), 473–486. https://doi.org/10.1175/JAS-D-22-0138.1

Rapp, M., Kaifler, B., Dörnbrack, A., Gisinger, S., Mixa, T., Reichert, R., et al. (2021). SOUTHTRAC-GW: An airborne field campaign to explore gravity wave dynamics at the world's strongest hotspot. *Bulletin of the American Meteorological Society*, *102*(4), E871–E893. https://doi.org/10.1175/BAMS-D-20-0034.1

Rocken, C., Kuo, Y. H., Schreiner, W. S., Hunt, D., Sokolovskiy, S., & McCormick, C. (2000). COSMIC system description. *Terrestrial, Atmospheric and Oceanic Sciences*, *11*(1), 21–52. https://doi.org/10.3319/TAO.2000.11.1.21(COSMIC)

Scherllin-Pirscher, B., Steiner, A. K., Anthes, R. A., Alexander, M. J., Alexander, S. P., Biondi, R., et al. (2021). Tropical temperature variability in the UTLS: New insights from GPS radio occultation observations. *American Meteorological Society*, *34*(8), 2813–2838. https://doi.org/10.1175/JCLI-D-20-0385.1

Scherllin-Pirscher, B., Steiner, A. K., Kirchengast, G., Kuo, Y.-H., & Foelsche, U. (2011). Empirical analysis and modeling of errors of atmospheric profiles from GPS radio occultation. *Atmospheric Measurement Techniques*, *4*(9), 1875–1890. https://doi.org/10.5194/amt-4-1875-2011

Schmidt, T., Alexander, P., & de la Torre, A. (2016). Stratospheric gravity wave momentum flux from radio occultations. *Journal of Geophysical Research: Atmospheres*, *121*(9), 4443–4467. https://doi.org/10.1002/2015JD024135

Scinocca, J. F., & McFarlane, N. A. (2000). The parametrization of drag induced by stratified flow over anisotropic orography. *Quarterly Journal of the Royal Meteorological Society*, *126*(568), 2353–2393. https://doi.org/10.1002/qj.49712656802

Shah, K., Solomon, S., Kinnison, D., Fu, Q., & Thompson, D. W. (2022). Phase unlocking and the modulation of tropopause-level trace gas advection by the quasibiennial oscillation. *Journal of Geophysical Research: Atmospheres*, *127*(21), e2021JD036142. https://doi.org/10.1029/2021JD036142

Smith, R. B., & Kruse, C. G. (2017). Broad-spectrum mountain waves. *Journal of the Atmospheric Sciences*, *74*(5), 1381–1402. https://doi.org/10.1175/JAS-D-16-0297.1

Smith, R. B., & Kruse, C. G. (2018). A gravity wave drag matrix for complex terrain. *Journal of the Atmospheric Sciences*, *75*(8), 2599–2613. https://doi.org/10.1175/JAS-D-17-0380.1

Solomon, S. (1999). Stratospheric ozone depletion: A review of concepts and history. *Reviews of Geophysics*, *37*(3), 275–316. https://doi.org/10.1029/1999RG900008

Solomon, S., Kinnison, D., Bandoro, J., & Garcia, R. (2015). Simulation of polar ozone depletion: An update. *Journal of Geophysical Research: Atmospheres*, *120*(15), 7958–7974. https://doi.org/10.1002/2015JD023365

Solomon, S., Kinnison, D., Garcia, R. R., Bandoro, J., Mills, M., Wilka, C., et al. (2016). Monsoon circulations and tropical heterogeneous chlorine chemistry in the stratosphere. *Geophysical Research Letters*, *43*(24), 12624–12633. https://doi.org/10.1002/2016GL071778

Stockwell, R., Mansinha, L., & Lowe, R. (1996). Localization of the complex spectrum: The S transform. *IEEE Transactions on Signal Processing*, *44*(4), 998–1001. https://doi.org/10.1109/78.492555

Stone, K. A., Solomon, S., Kinnison, D. E., Baggett, C. F., & Barnes, E. A. (2019). Prediction of Northern Hemisphere regional surface temperatures using stratospheric ozone information. *Journal of Geophysical Research: Atmospheres*, *124*(12), 5922–5933. https://doi.org/10.1029/2018JD029626

Tabazadeh, A., Turco, R. P., & Jacobson, M. Z. (1994). A model for studying the composition and chemical effects of stratospheric aerosols. *Journal of Geophysical Research*, *99*(D6), 12897–12914. https://doi.org/10.1029/94JD00820

Taylor, M. J., Pautet, P. D., Fritts, D. C., Kaifler, B., Smith, S. M., Zhao, Y., et al. (2019). Large-amplitude mountain waves in the mesosphere observed on 21 June 2014 during DEEPWAVE: 1. Wave development, scales, momentum fluxes, and environmental sensitivity. *Journal of Geophysical Research: Atmospheres*, *124*(19), 10364–10384. https://doi.org/10.1029/2019JD030932

Toon, G. C., Farmer, C. B., Lowes, L. L., Schaper, P. W., Blavier, J.-F., & Norton, R. H. (1989). Infrared aircraft measurements of stratospheric composition over Antarctica during September 1987. *Journal of Geophysical Research*, *94*(D14), 16571–16596. https://doi.org/10.1029/JD094iD14p16571

UCAR COSMIC Program. (2006). COSMIC-1 data products [Dataset] (Tech. Rep.). UCAR/NCAR - COSMIC. https://doi.org/10.5065/ZD80-KD74

Vosper, S. B., van Niekerk, A., Elvidge, A., Sandu, I., & Beljaars, A. (2020). What can we learn about orographic drag parametrisation from high-resolution models? A case study over the Rocky Mountains. *Quarterly Journal of the Royal Meteorological Society*, *146*(727), 979–995. https://doi.org/10.1002/QJ.3720

Wang, L., & Alexander, M. J. (2010). Global estimates of gravity wave parameters from GPS radio occultation temperature data. *Journal of Geophysical Research*, *115*(D21), D21122. https://doi.org/10.1029/2010JD013860

Wang, M., & Penner, J. E. (2010). Cirrus clouds in a global climate model with a statistical cirrus cloud scheme. *Atmospheric Chemistry and Physics*, *10*(12), 5449–5474. https://doi.org/10.5194/acp-10-5449-2010

Wegner, T., Kinnison, D. E., Garcia, R. R., & Solomon, S. (2013). Simulation of polar stratospheric clouds in the specified dynamics version of the whole atmosphere community climate model. *Journal of Geophysical Research: Atmospheres*, *118*(10), 4991–5002. https://doi.org/10.1002/jgrd.50415

Weimer, M., Buchmüller, J., Hoffmann, L., Kirner, O., Luo, B., Ruhnke, R., et al. (2021). Mountain-wave-induced polar stratospheric clouds and their representation in the global chemistry model ICON-ART. *Atmospheric Chemistry and Physics*, *21*(12), 9515–9543. https://doi.org/10.5194/ACP-21-9515-2021

Weimer, M., Wilka, C., Kinnison, D. E., Garcia, R. R., Bacmeister, J. T., Alexander, M. J., et al. (2023). A method for estimating global subgrid-scale orographic gravity-wave temperature perturbations in chemistry-climate models [Dataset]. Retrieved from https://www.acom.ucar.edu/DOI-DATA/dkin/JAMES_Weimer_2022

Wright, C. J. (2019). Quantifying the global impact of tropical cyclone-associated gravity waves using HIRDLS, MLS, SABER and IBTrACS data. *Quarterly Journal of the Royal Meteorological Society*, *145*(724), 3023–3039. https://doi.org/10.1002/QJ.3602

Xu, J., Smith, A. K., & Brasseur, G. P. (2000). The effects of gravity waves on distributions of chemically active constituents in the mesopause region. *Journal of Geophysical Research*, *105*(D21), 26593–26602. https://doi.org/10.1029/2000JD900446

Xu, J., Smith, A. K., & Ma, R. (2003). A numerical study of the effect of gravity-wave propagation on minor species distributions in the mesopause region. *Journal of Geophysical Research*, *108*(D3), 4119. https://doi.org/10.1029/2001JD001570

Zou, L., Hoffmann, L., Griessbach, S., Spang, R., & Wang, L. (2021). Empirical evidence for deep convection being a major source of stratospheric ice clouds over North America. *Atmospheric Chemistry and Physics*, *21*(13), 10457–10475. https://doi.org/10.5194/ACP-21-10457-2021